

GEORGIA DOT RESEARCH PROJECT 19-21

Final Report

**USE OF GROUND PENETRATING
RADAR TECHNOLOGY TO ASSESS AND
MONITOR PAVEMENT STRUCTURAL
CONDITIONS FOR IMPROVED
PAVEMENT MAINTENANCE AND
REHABILITATION STRATEGIES**



Office of Performance-based Management and Research
600 West Peachtree Street NW | Atlanta, GA 30308

September 2021

TECHNICAL REPORT DOCUMENTATION PAGE

1. Report No.: FHWA-GA-21-1921	2. Government Accession No.: N/A	3. Recipient's Catalog No.: N/A	
4. Title and Subtitle: Use of Ground Penetrating Radar Technology to Assess and Monitor Pavement Structural Conditions for Improved Pavement Maintenance and Rehabilitation Strategies		5. Report Date: September 2021	
		6. Performing Organization Code: N/A	
7. Author(s): S. Sonny Kim, Ph.D., P.E.; Stephan A. Durham, Ph.D., P.E.; J. James Yang, Ph.D., P.E.; Ahmad Abdelmawla. M.S.; Ryan Romeo		8. Performing Organization: Report No.: 19-21	
9. Performing Organization Name and Address: University of Georgia, College of Engineering Driftmier Engineering Center 597 DW Brooks Drive Athens, GA 30602 Phone: (706) 542-9804 Email: kims@uga.edu		10. Work Unit No.: N/A	
		11. Contract or Grant No.: PI# 0016970	
12. Sponsoring Agency Name and Address: Georgia Department of Transportation (SPR) Office of Performance-based Management and Research 600 West Peachtree Street NW Atlanta, GA 30308		13. Type of Report and Period Covered: Final Report (Nov. 2019–Sept. 2021)	
		14. Sponsoring Agency Code: N/A	
15. Supplementary Notes: Prepared in cooperation with the U.S. Department of Transportation, Federal Highway Administration			
16. Abstract: <p>Ground-penetrating radar (GPR) technology has been widely applied in ground subsurface investigations. The major development of GPR for pavement assessment originated in the early 1980s and since has become a well-established investigation technique for pavements. Analysis of GPR data provides much richer information on layer depths of pavement structure, material conditions, moisture content, voids, and locations of reinforcement and other features. Being able to accurately and reliably assess the underlying conditions of pavements is essential to fully understand both functional and structural deficiencies or failures of pavements and associated causality. This improved understanding will lead to the most cost-effective maintenance and rehabilitation treatments and considerable savings in maintenance and rehabilitation expenditure.</p> <p>The overall goal of this research is to extend the GPR technology in combination with modern data analytics to provide improved pavement investigation capabilities. As a result, new methodologies and analytical procedures were developed to acquire and analyze field GPR data, and infer subgrade density and water content, which are critical for the diagnosis of pavement failure and underlying causality. Based on the outcomes of the research, the potential pavement foundation issues of critical state highways in Georgia are reported.</p> <p>This study also compares GPR and falling weight deflectometer (FWD) data. Analysis of the preliminary results from I-75N suggest GPR is capable of identifying general trends in the variation of subgrade density and modulus. However, a further investigation into the relationship between GPR-derived subgrade density and FWD- back calculated subgrade modulus is recommended. The expected benefit of determining an accurate relationship between the two methodologies is that GPR can be used as an initial investigation, which can quickly identify locations of atypical/abnormal/unexpected pavement characteristics. Then, FWD testing can be conducted at those locations and serve as a deeper investigation, which takes more time to conduct/process but has higher accuracy.</p>			
17. Key Words: Ground Penetrating Radar, Soil Density, NDT, Resilient		18. Distribution Statement: No Restriction	
19. Security Classification(of this report): Unclassified	20. Security Classification (of this page): Unclassified	21. No. of Pages: 94	22. Price: Free

GDOT Research Project 19-21

Final Report

USE OF GROUND PENETRATING RADAR TECHNOLOGY TO ASSESS AND MONITOR
PAVEMENT STRUCTURAL CONDITIONS FOR IMPROVED PAVEMENT MAINTENANCE
AND REHABILITATION STRATEGIES

By

S. Sonny Kim, Ph.D., P.E.
Associate Professor

Stephan A. Durham, Ph.D., P.E.
Professor

J. James Yang, Ph.D., P.E.,
Associate Professor

Ahmad Abdelmawla, M.S.
Graduate Research Assistant

Ryan Romeo, B.S.
Graduate Research Assistant

University of Georgia Research Foundation, Inc.

Contract with
Georgia Department of Transportation

In cooperation with
U.S. Department of Transportation, Federal Highway Administration

September 2021

The contents of this report reflect the views of the authors who are responsible for the facts and the accuracy of the data presented herein. The contents do not necessarily reflect the official views or policies of the Georgia Department of Transportation or the Federal Highway Administration. This report does not constitute a standard, specification, or regulation.

SI* (MODERN METRIC) CONVERSION FACTORS				
APPROXIMATE CONVERSIONS TO SI UNITS				
Symbol	When You Know	Multiply By	To Find	Symbol
LENGTH				
in	inches	25.4	millimeters	mm
ft	feet	0.305	meters	m
yd	yards	0.914	meters	m
mi	miles	1.61	kilometers	km
AREA				
in ²	square inches	645.2	square millimeters	mm ²
ft ²	square feet	0.093	square meters	m ²
yd ²	square yard	0.836	square meters	m ²
ac	acres	0.405	hectares	ha
mi ²	square miles	2.59	square kilometers	km ²
VOLUME				
fl oz	fluid ounces	29.57	milliliters	mL
gal	gallons	3.785	liters	L
ft ³	cubic feet	0.028	cubic meters	m ³
yd ³	cubic yards	0.765	cubic meters	m ³
NOTE: volumes greater than 1000 L shall be shown in m ³				
MASS				
oz	ounces	28.35	grams	g
lb	pounds	0.454	kilograms	kg
T	short tons (2000 lb)	0.907	megagrams (or "metric ton")	Mg (or "t")
TEMPERATURE (exact degrees)				
°F	Fahrenheit	5 (F-32)/9 or (F-32)/1.8	Celsius	°C
ILLUMINATION				
fc	foot-candles	10.76	lux	lx
fl	foot-Lamberts	3.426	candela/m ²	cd/m ²
FORCE and PRESSURE or STRESS				
lbf	poundforce	4.45	newtons	N
lbf/in ²	poundforce per square inch	6.89	kilopascals	kPa
APPROXIMATE CONVERSIONS FROM SI UNITS				
Symbol	When You Know	Multiply By	To Find	Symbol
LENGTH				
mm	millimeters	0.039	inches	in
m	meters	3.28	feet	ft
m	meters	1.09	yards	yd
km	kilometers	0.621	miles	mi
AREA				
mm ²	square millimeters	0.0016	square inches	in ²
m ²	square meters	10.764	square feet	ft ²
m ²	square meters	1.195	square yards	yd ²
ha	hectares	2.47	acres	ac
km ²	square kilometers	0.386	square miles	mi ²
VOLUME				
mL	milliliters	0.034	fluid ounces	fl oz
L	liters	0.264	gallons	gal
m ³	cubic meters	35.314	cubic feet	ft ³
m ³	cubic meters	1.307	cubic yards	yd ³
MASS				
g	grams	0.035	ounces	oz
kg	kilograms	2.202	pounds	lb
Mg (or "t")	megagrams (or "metric ton")	1.103	short tons (2000 lb)	T
TEMPERATURE (exact degrees)				
°C	Celsius	1.8C+32	Fahrenheit	°F
ILLUMINATION				
lx	lux	0.0929	foot-candles	fc
cd/m ²	candela/m ²	0.2919	foot-Lamberts	fl
FORCE and PRESSURE or STRESS				
N	newtons	0.225	poundforce	lbf
kPa	kilopascals	0.145	poundforce per square inch	lbf/in ²

* SI is the symbol for the International System of Units. Appropriate rounding should be made to comply with Section 4 of ASTM E380. (Revised March 2003)

TABLE OF CONTENTS

EXECUTIVE SUMMARY	1
CHAPTER 1. INTRODUCTION.....	3
BACKGROUND	4
Pavement Structures.....	4
Ground Penetrating Radar	6
PROBLEM STATEMENT	7
RESEARCH OBJECTIVES	8
RESEARCH SIGNIFICANCE AND SCOPE	8
CHAPTER 2. LITERATURE REVIEW.....	9
OVERVIEW	9
NONDESTRUCTIVE TESTING APPLICATIONS	9
ELECTROMAGNETIC TESTING TECHNOLOGY	10
GROUND PENETRATING RADAR	11
Ground-Coupled vs. Air-Coupled Antennas.....	13
Electromagnetic Theory for GPR	14
GPR Interpolations.....	20
CHAPTER 3. MODEL DERIVATION AND IMPLEMENTATION.....	22
OBJECTIVE.....	22
THEORETICAL BACKGROUND.....	22
DENSITY PREDICTION MODEL	23
Relationship between water content & permittivity.....	25
MODEL IMPLEMENTATION	25
MODEL CALIBRATION	26
CHAPTER 4. MODEL VALIDATION FOR SUBGRADE DENSITY	27
LABORATORY TEST	27
Physical Properties Testing.....	28
Laboratory Sand Cone Test	29
GPR Calibration	30
Laboratory GPR Scan Results.....	31
FIELD VALIDATION.....	36
GPR Scanning	39
Field Verification Test Results.....	40
CHAPTER 5. RELATIONSHIP BETWEEN SUBGRADE DENSITY AND MODULUS FROM FALLING WEIGHT DEFLECTOMETER	43
INTRODUCTION.....	43

FWD BACK CALCULATION BACKGROUND..... 43
 Numerical Pavement Models 44
 Optimization Routines..... 46
DESCRIPTION OF BACK CALCULATION SOFTWARE..... 47
METHOD..... 48
RESULTS AND DISCUSSION 49
SUMMARY 52
CHAPTER 6. NETWORK-LEVEL FIELD GPR DATA ACQUISITION AND ANALYSIS 53
 I-20 GPR SCAN RESULTS 55
 I-75 GPR SCAN RESULTS 57
 I-85 GPR SCAN RESULTS 60
 I-285 GPR SCAN RESULTS 64
CHAPTER 7. CONCLUSIONS AND RECOMMENDATIONS..... 75
 CONCLUSIONS 75
 RECOMMENDATIONS 76
APPENDIX A. PROPOSED GDT TEST METHOD..... 77
ACKNOWLEDGMENTS..... 81
REFERENCES 82

LIST OF FIGURES

Figure 1. Chart. Pavement structure diagram ⁽⁴⁾	5
Figure 2. Chart. GPR theoretical application flowchart ⁽²⁵⁾	12
Figure 3. Photo. UGA GPR System photo: (a) GSSI 2 GHz air-coupled antenna, (b) GSSI 400 MHz ground-coupled antenna.....	13
Figure 4. Chart. Multi layered system diagram of GPR signal reflection.....	20
Figure 5. Chart. Soil phase diagram.....	24
Figure 6. Chart. GPR–dry density model implementation.....	26
Figure 7. Photos. Sample preparation photos: (a) Soil transportation and filling testing box, (b) soil compaction.....	27
Figure 8. Photo. divided soil samples.	28
Figure 9. Photo. laboratory sand cone test.	29
Figure 10. Photo. GPR Scanning and calibration for different samples.	30
Figure 11. Graph. Amplitude from metal plate calibration.....	31
Figure 12. Graphs. Amplitude for different soil samples.....	33
Figure 13. Graph. Comparison between measured and calculated soil dry densities.	34
Figure 14. Graph. Exponential model vs measured soil bulk density.....	35
Figure 15. Photo. Field verification test 1 aerial photo.....	36
Figure 16. Photo. Field verification test 2 aerial photo.....	37
Figure 17. Photo. Field verification test 3 aerial photo.....	37
Figure 18. Photo. Sand cone test for SR 53 test section.....	38
Figure 19. Photo. UGA GPR van.....	39
Figure 20. Photo. UGA GPR road survey control units.....	39
Figure 21. Graph. Calculated dry density for SR 53.....	40
Figure 22. Graph. Calculated dry density for West Winder Pass.....	41
Figure 23. Graph of Calculated dry density for SR 316.....	42
Figure 24. Graph. Comparison graph between the subgrade soil densities calculated from the raw GPR data (black) and its moving average (red).....	50
Figure 25. Graph. Comparison graph between the moving-averaged subgrade density calculated from GPR data (black) and the FWD-back calculated subgrade modulus from UGA-PAVE (red).....	51
Figure 26. Map. scanned critical state routes in District 7.....	54
Figure 27. Graph. Estimated Subgrade soil density for I-20 (EB – slow lane).....	55
Figure 28. Map. I-20 scan (EB - slow lane).....	56
Figure 29. Graph. Subgrade soil density distribution for I-75 (NB – slow lane).....	57
Figure 30. Map. I-75 scan (NB – slow lane).....	58
Figure 31. Graph. subgrade soil density distribution for I-75 (SB – slow lane).	59
Figure 32. Map. I-75 scan (SB – slow lane).....	60
Figure 33. Graph. Subgrade soil density distribution for I-85 (SB – slow lane).....	61
Figure 34. Map. I-85 scan (SB – slow lane).....	62
Figure 35. Graph. Subgrade soil density graph for I-85 (NB – slow lane).	63
Figure 36. Map. I-85 scan (NB – slow lane).....	63
Figure 37. Graph. Subgrade soil density graph for I-285 (inner loop).....	64
Figure 38. Map. I-285 scan (inner loop)	65
Figure 39. Graph. Subgrade soil density graph for I-285 (outer loop).....	66
Figure 40. Map. I-285 scan(outer loop)	67
Figure 41. Map. weak spots for critical state routes in District 7 – Slow lane.....	68
Figure 42. Chart. Density Model Implementation	78

LIST OF TABLES

Table 1. Soil specimen index properties.	28
Table 2. Laboratory sand cone test results.	29
Table 3. Dielectric constant results.	31
Table 4. Proposed model calculation results.	32
Table 5. Comparison between proposed model and sand cone test results.	34
Table 6. Exponential model results.	35
Table 7. Verification field tests.	36
Table 8. SR 53 sand cone test results.	38
Table 9. West Winder Pass sand cone test results.	38
Table 10. SR 316 sand cone test results.	39
Table 11. Sand cone test results for SR 53.	40
Table 12. Sand cone test results for West Winder Pass.	41
Table 13. Sand cone test results for SR 316.	41
Table 14. Start/End coordinates of tested sections.	53
Table 15. I-20 (eastbound – slow lane) sections summary.	55
Table 16. I-75 (northbound – slow lane) sections summary.	57
Table 17. I-75 (southbound – slow lane) sections summary.	59
Table 18. I-85 (southbound – slow lane) sections summary.	61
Table 19. I-85 (northbound – slow lane) sections summary.	62
Table 20. I-285 (inner loop – slow lane) sections summary.	64
Table 21. I-285 (outer loop – slow lane) sections summary.	66
Table 22. Critical sections output example.	69

EXECUTIVE SUMMARY

In situ subgrade density is critical to the performance of flexible pavements, as it is directly related to the pavement's structural capacity. Through this study, a methodology to assess the dry density of in situ subgrade soil was developed using ground penetrating radar (GPR) technology. The GPR scans were performed for the critical state routes in District 7 at the highway speed, and the GPR data were utilized to estimate the subgrade density. This report aims to help pavement engineers understand the application of GPR in the estimation of subgrade soil density as well as assist with on-site pavement condition assessments.

In this study, a prediction model for subgrade soil density was developed using the dielectric constant, which GPR can measure, and the electromagnetic (EM) mixing theory. The developed model was first evaluated using lab soil samples with the controlled density and water content. The GPR density model was further validated using field data collected from three construction sites in Georgia. It was found that the prediction accuracy of the GPR was comparable to, or better than, that of the traditional sand cone test. For the subgrade soils with lower water content, the average density prediction errors of GPR were between 0.02 and 5.00 percent.

A total of 570 miles was scanned with GPR in the slow lanes of critical state routes in District 7. Based on the data analysis, it is concluded that:

- Permittivity measurements can effectively infer subsurface moisture content from GPR.
- The proposed semi-empirical model for subgrade dry density prediction is appropriate for the test sections. The relationship overestimates the expected dry density for higher water content values, independently from soil texture. Thus, the prediction is more accurate for low-moisture soils within the entire range of soils surveyed.

- The relative dielectric permittivity increases as a function of density value. In other words, the greater the material is compacted, the higher its relative permittivity.
- The predicted subgrade density matches well with the observed subgrade density based on lab and field test results. Overall, the errors are lower than 11 percent in most of the surveyed stations.
- The trends in subgrade density predicted from the GPR density model are similar to those in subgrade modulus back calculated from GPR. This suggests GPR has the potential to identify locations with weak subgrade, which can help with site selection for FWD testing.

In addition, the following recommendations are provided:

- Caution must be exercised when averaging GPR traces to be used as a reference signal for representing the investigated medium's deformations. It is highly recommended to have full knowledge of the instrument's influence domain for the measurement of dry density.
- Future research may be focused on a different range of frequencies to estimate subgrade soils' strength using GPR.
- Periodic GPR scanning for the test sections is recommended to establish a reliable data source that could be used with deep learning techniques for improving subgrade diagnosis capability.
- Analysis of the preliminary results from I-75N suggest GPR can identify trends in variation of subgrade density and modulus. However, deeper investigation into the relationship between GPR-derived subgrade density and FWD back calculated subgrade modulus is recommended. The expected benefit of correlating the two methods is that GPR can be used as an initial screening to quickly identify locations of a typical/abnormal/unexpected pavement characteristics. Then, FWD testing can be conducted at the selected locations for deeper investigation.

CHAPTER 1. INTRODUCTION

Subgrade density is one of the essential components for a structurally sound pavement system. In the field, subgrades soils are compacted to a desirable level to provide a robust platform for pavement layers. Insufficient field compaction is the most frequent construction-related issue resulting in lower subgrade density and potential structural failure.

Traditionally, the sand cone test and nuclear density gauge methods have been widely used to estimate in-place subgrade soil density. Sand cone test requires access to the subgrade soil to directly measure the soils' volumetric properties. Although this method provides accurate measurements, it only provides a minimal number of measurements and is time-consuming due to the relatively slow procedures for testing.

The nuclear gauge is a nondestructive technique that provides accurate estimates of the density. However, the nuclear gauge technique provides limited information about the layer density since nuclear measurements are usually taken with high spatial distances. Also, a nuclear gauge operation uses radioactive materials and should only be conducted by authorized personnel with special licensing.

Electromagnetic (EM) density gauges have recently been introduced as an alternative to the nuclear density gauges. These nonnuclear devices use EM signals to measure in situ density. Such EM density gauges eliminate the need for licenses, training, and specialized storage, as well as the risks associated with devices that use a radioactive source ⁽¹⁾. However, unlike traditional methods, the nonnuclear density gauges do not provide continuous test results for the entire pavement area.

Determining field subgrade conditions in pavement requires a specified number of samples regardless of the density measurement method used. The sample-based assessment is only performed at limited spots and may not represent the entire surveyed road section. Further, a spot test may need traffic control during the test, which may cause traffic congestion. Therefore, a rapid and reliable test method that covers expansive surface areas becomes necessary to enhance the level of confidence in the evaluation. This study proposes a prediction model to estimate in-place subgrade dry density using ground penetrating radar (GPR), which is fast, continuous, and reliable. Besides the subgrade density estimation, the GPR tests provide additional information about pavement structures, such as layer thickness.

BACKGROUND

Pavement Structures

A ‘pavement’ is defined as an engineered structure designed to carry vehicle loads, and the importance of well-built and maintained pavement structures has long been recognized. Some of the earliest examples of pavement structures include stone-paved streets in the Middle East, wooden log-surfaced roads in England, dating from around 4000 B.C., and brick paving used in India about 3000 B.C.⁽¹⁾. Historically, the most famous use of sound pavement engineering was by the Roman Empire, which contained a network of approximately 78,000 km of paved roads at its peak ⁽²⁾. Rome’s practice of constructing roads on raised embankments (to allow a better view of the surrounding area) gave rise to the term “highway.”

While the purpose of modern pavement structures is to carry vehicles, pavement type depends on the road utilized application, which is vital for the infrastructure, development, and economy of countries around the globe. Modern pavement structures consist of several elements ⁽³⁾, and defines pavement’s

functions as providing a safe, stable, and durable design while under the action of both the weather and the loading imposed by vehicles.

Pavement structures consist of several layers of materials placed over the natural ground ('subgrade'), as illustrated in figure 1. Above the subgrade is the subbase, which is usually a layer of unbound compacted aggregate to protect the subgrade from cold weather action and provide a platform for constructing the upper pavement layers. Sometimes a 'capping' layer is also included below the subbase, consisting of lower grade compacted unbound aggregate. The subbase, capping (if present), and subgrade are together considered to be the pavement structure's foundation.

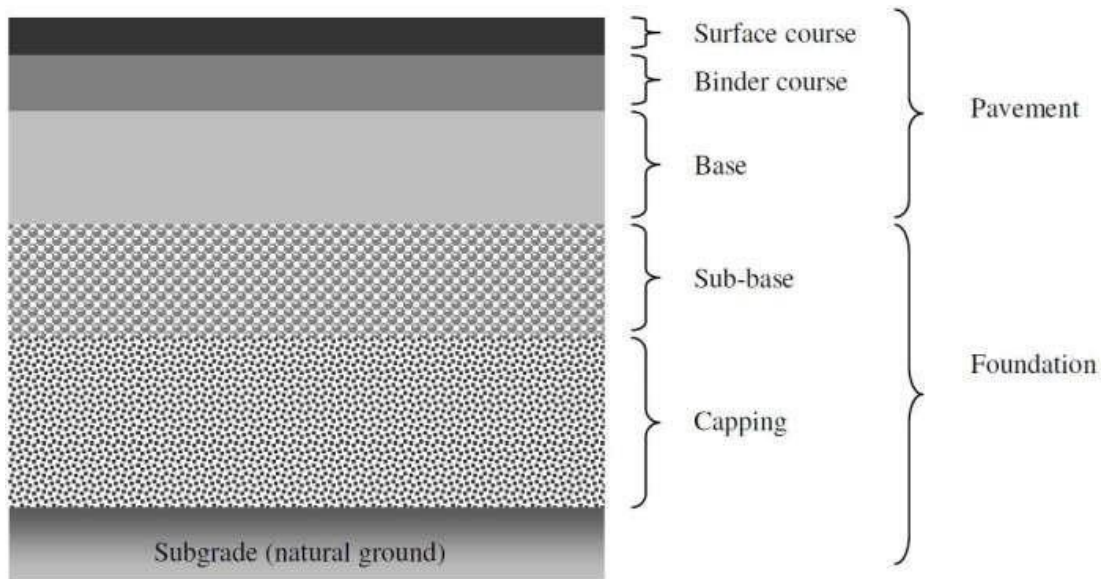


Figure 1. Chart. Pavement structure diagram ⁽⁴⁾.

Above the subbase, the pavement's main structural layer, known as the 'base' (or 'road base'), is constructed. This base usually consists of a selected crushed rock material bound together with bitumen to form an asphalt layer or cement to form a cement-bound material (CBM) layer. The base layer is designed to withstand the loadings placed on the pavement by vehicles and to distribute them so that the foundation materials do not become damaged.

Above the base layer is the pavement surfacing, which is often provided in two bound material layers, known as the 'binder course' and the 'surface course'. The binder course is, in effect, an extension of the base layer. It provides a regulating system upon which the uppermost surface course layer is placed to provide a comfortable and safe surface for vehicles. When bitumen-bound material (asphalt) only is used in the pavement, each layer consists of a slightly different mix of aggregate and bitumen best suited to perform the function required. However, when the pavement is constructed from CBM only, the role of all the bound layers (surface course, binder course, and base) is provided by a single concrete slab (which sometimes may contain steel reinforcement).

Pavements that consist of only asphalt materials are known as 'flexible' pavements, and those with CBM only are termed 'rigid' pavements. Some pavements, significantly rehabilitated ones, are designed with a CBM base layer and asphalt surfacing, and these are referred to as 'composite' pavements.

Ground Penetrating Radar

The use of radar (i.e., radio detection and ranging) for determining the distance of objects was initially developed in the first half of the twentieth century, with arguably its most well-known early use being the range-finding of aircraft during World War II. However, attempts had been made in the 1920's and 30's to use rudimentary radar technology to measure the depths and thicknesses of ice sheets and glaciers. As electronics and technology developed, the use of radar technology for determining properties of other ground materials took place. Still, it was not until the 1960's that the technique began to gain use for relatively short distances in the ground, and the first application of what, by then, had become known as 'ground penetrating radar' on road structures took place in the 1970's and 80's.

The initial application of GPR to pavement structures focused on determining depths within the pavement, such as material layer thicknesses. Subsequently, the use of GPR data to obtain information on other pavement properties began to develop. By further investigating the response of pavement materials to the passage of radar signals within pavement structures, additional information regarding material properties such as the location of discrete features and water and air presence (voids) could also be determined and communicated to the pavement engineer.

Several GPR system types exist based on the same physical principles of electromagnetic (EM) wave propagation, but they employ different hardware, software, and data processing procedures. The most popular and commercially available GPR systems are the “impulse” type, which transmits a short pulse of electromagnetic energy and records the time taken, amplitude, and phase of reflections of the pulse to return to the antenna. Impulse GPR surveys on pavements are usually conducted by collecting data along survey lines, consisting of individual radar pulses recorded at a constant spacing along the length of the survey line.

PROBLEM STATEMENT

Currently, the Georgia Department of Transportation (GDOT) is facing a need to define and understand pavement structure type, individual layer thicknesses, field soils’ density, as well as potential structural causations for pavement distresses along each surveyed lane with corresponding GPS coordinates and mileposts to investigate existing pavement profile and to develop a feasible maintenance and rehabilitation strategy.

The University of Georgia (UGA) research team has developed an air-coupled vehicle-mounted GPR system that uses an antenna frequency between 400MHz to 2.0 GHz. The UGA’s GPR system continuously captures a pavement subsurface profile with continuous video recording (CVR) of surface images, pavement profile, and a potential structural failure (e.g., sinkholes, rock faulting) at

the posted speed limit (45 mph to 65 mph) without any traffic controls.

RESEARCH OBJECTIVES

The objectives of this research project are to:

- (1) Establishes a GIS/GPS/CVR enabled map including locations (from GIS), pavement profiles (from GPR), estimated subgrade dry density, and surface images (from CVR) for critical state routes in District 7 in Georgia
- (2) to provide a reliable condition assessment and pavement distress evaluation tool for a cost-effective maintenance program
- (3) to identify potential problematic areas based on field GPR survey data and image analyses

RESEARCH SIGNIFICANCE AND SCOPE

The primary benefit of this study is the identification of both pavement profile information and surface conditions simultaneously for major highway systems in Georgia, which will be helpful in many roadway-related investigations. Also, the subgrade density map that is developed through this research will provide appropriate supporting information to diagnose the subsurface condition of subgrade density and pavement performance. As such, the map with field-measured subsurface and surface data will become an invaluable asset for reliable pavement condition evaluation, maintenance, and rehabilitation.

CHAPTER 2. LITERATURE REVIEW

OVERVIEW

Over the last decades, road engineer activities have focused on properly managing existing infrastructural assets through effective and efficient maintenance actions rather than constructing new roads.

A range of techniques can be used to determine information about pavement conditions. Those techniques that can obtain information without damaging the pavement (i.e., nondestructive testing [NDT]) have a distinct advantage, and wherever possible, they tend to be favored for pavement investigations. The main methods for structural assessment of pavement materials include falling weight deflectometer (FWD), GPR, coring of the pavement material, and excavating test pits (also known as ‘trial pits’) with laboratory testing of core or trial pit samples. Of these options, FWD and GPR offer engineers advantages in that they are both NDT methods.

Obtaining measurements of the deflections of road pavements under loads, such as with the FWD, is currently one of the main criteria for assessing pavements’ long-term performance. Transport and Road Research Laboratory (TRL) Report LR 833 ⁽⁵⁾, detailed the relationship between deflection and predicted future pavement performance. Measured deflections and known traffic loading of pavement can be used to predict how long the pavement will take (the ‘residual life’) to reach the point at which strengthening will be required to prolong its useful life.

NONDESTRUCTIVE TESTING APPLICATIONS

Detection and classification of defects and damages in the investigated media are the main aims of NDT or nondestructive evaluation (NDE) methods ⁽⁶⁾, although it is not always possible to quantify

their magnitude. Such aims include determining the position and dimensions of heterogeneities when changes in physical properties inside a homogeneous domain occur.

Over recent years, repair and maintenance of existing structures are being planned through various investigations using these techniques. The most common include concrete testing ^(7,8,9), inspection for ancient building safeguards ^(10,11), for land use purposes ^(12,13), modern infrastructures safety, characterization of stone masonries ^(14,15,16,17), and bridge deck inspections ^(18,19,20).

In pavement engineering, driving safety is strictly related to pavement surface conditions ⁽²¹⁾. Cracks, potholes, and surface deformations generate sudden vertical accelerations on the vehicle tires, thereby decreasing the effective friction between tires and pavement. Such road damages are related to the low bearing ratio of subgrade soils ⁽²²⁾. Previous research has demonstrated that structural damage in road pavement depends on the moisture percentage in sub-asphalt courses ⁽²³⁾. As of today, conventional destructive methods are still needed for calibrating measurements by NDTs, although technological and research advances are increasingly limiting the use of core samples ⁽⁶⁾.

ELECTROMAGNETIC TESTING TECHNOLOGY

The analysis of propagation velocity of electromagnetic (EM) waves in materials is the primary method that underlies EM techniques. EM methods rely on the transmission/reflection of short electromagnetic impulses, with antenna systems capable of emitting and detecting them. Dielectric permittivity is the parameter that controls the propagation velocity, and in this respect, moisture content highly influences its value. The conductivity and dielectric losses affect the attenuation of the electromagnetic wave energy.

The passage of radar signals through materials is governed by the physical laws concerning EM waves. EM waves are alternating electrical and magnetic fields that propagate out from an oscillating

electrical charge. Many different types of EM waves compose the entire EM spectrum. Other EM wave types are characterized by their frequency, which is measured by the number of cycles per second (Hz) of the electrical and magnetic fields. The frequency of the wave, together with the speed at which it travels through a material, determines its wavelength. The EM wave spectrum includes, at the highest frequency, gamma waves with wavelengths of the order of 0.01 nm (0.01×10^{-9} m), down to radio waves at the lowest frequency with wavelengths in the order of 1.0 km. Although the acronym ‘radar’ is referred to initially as radio frequency waves, modern GPR systems operate at the lower end of the microwave frequency range, with wavelengths in the order of a few cm.

A dielectric substance refers to one that does not conduct electricity well, but that does support electric fields. The response of a material to an EM wave is a function of the material’s dielectric properties, namely its electrical permittivity (ϵ), magnetic permeability (μ), and electrical conductivity (σ).

GROUND PENETRATING RADAR

The early 1980’s witnessed the first significant development of GPR for pavement applications, and it is now an established technique in many countries. GPR was first used in traffic infrastructure surveys in the 1970s by the U.S. Federal Highway Administration (FHWA) for testing in tunnel applications ⁽⁷⁾. Later, in 1985, the FHWA developed the first vehicle mounted GPR system for highway applications. GPR has been used successfully for several purposes in pavement investigation to obtain important pavement information. The major strengths of using GPR are its nondestructive nature in relation to road surveys, notably lower costs than traditional methods, high-speed and continuous data acquisition, and reliability. GPR provides accurate and high-resolution data compared to competing geophysical technologies such as seismic, transient electromagnetic, electrical, and magnetic approaches. However, its main performance limitations occur in the presence of high-conductivity materials, such as clay or salt- contaminated soils, and heterogeneous

conditions causing complicated electromagnetic-scattering phenomena.

In the civil engineering field, GPR is currently used for inspection, monitoring, and design purposes. The main applications include detecting utilities and buried objects, surveying road pavements, bridge decks, tunnels, and moisture content measurement in natural soils and artificial materials. Specifically, GPR has been successfully applied to obtain the pavement layer thickness and detect subsurface defects. The standard GPR systems are based on impulse frequencies that use a single electromagnetic wave at a selected frequency.

The foundations of GPR lie in EM theory. The history of this field spans more than two centuries and is the subject of numerous texts. This overview outlines the basic building blocks needed to work quantitatively with GPR, as shown in figure 2.

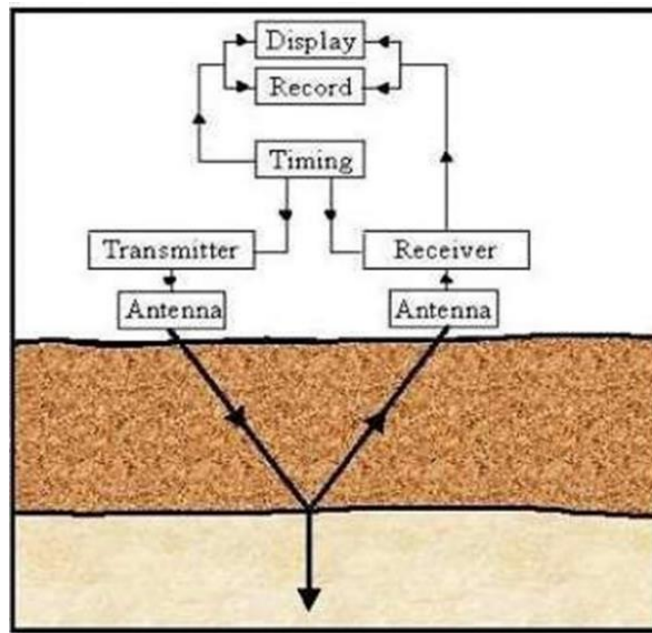


Figure 2. Chart. GPR theoretical application flowchart ⁽²⁵⁾.

Although all GPR systems operate by the EM wave principles described above, different types of GPR systems exploit slightly different aspects of EM wave propagation and use different hardware and data processing procedures.

The main components of an impulse GPR system (shown in figure 2) consist of an antenna unit (with transmitter and receiver), a control unit, a data console/display, and a power unit. Impulse GPR systems operate by transmitting a brief EM burst or ‘pulse’ from a transmitter and recording the pulse reflections from features or layers within the pavement as they are returned to a receiver.

Ground-Coupled vs. Air-Coupled Antennas

Several types of antennas exist for GPR, and the most used for impulse systems are ‘dipole’ or ‘bow-tie’. These require contact with the pavement surface (known as ground-coupled) to be most effective, but the ‘horn’ type can operate while suspended a short distance above the pavement surface (air-coupled). Figure 3 shows both types, air-coupled and ground-coupled antennas.

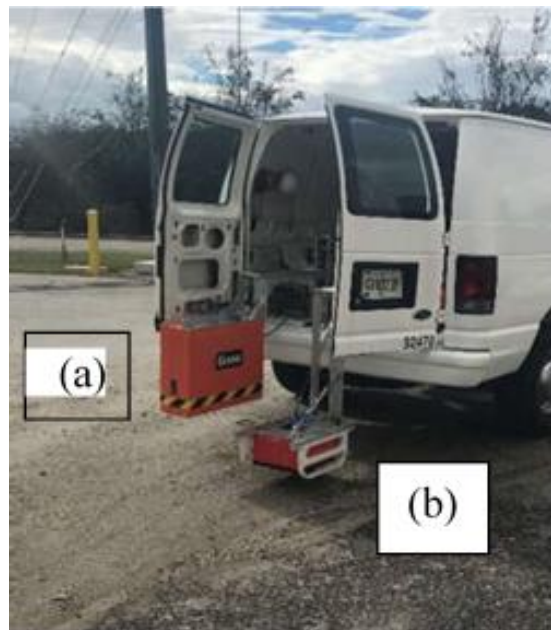


Figure 3. Photo. UGA GPR System photo: (a) GSSI 2 GHz air-coupled antenna, (b) GSSI 400 MHz ground-coupled antenna.

Ground-coupled antennas provide greater depth penetration (for a given signal frequency) and are physically smaller in size. However, air-coupled horn antennas allow higher scan and data acquisition rates and thus facilitate higher speed surveys. For a given signal frequency, air-coupled horn antennas

may prove the most appropriate when the upper layers of pavement are of most interest. Ground-coupled antennas may be more suitable where thicker pavements are encountered (e.g., airports) or where information about the pavement foundation is also required.

Electromagnetic Theory for GPR

Maxwell's equations mathematically describe the physics of EM fields, while constitutive relationships quantify material properties. Combining the two provides the foundations for quantitatively describing GPR signals.

In mathematical terms, EM fields and relationships are expressed as in equations 1, 2, and 3:

$$\nabla \cdot \bar{E} = -\frac{\partial \bar{B}}{\partial t} \quad (1)$$

$$\nabla \cdot \bar{D} = q \quad (2)$$

$$\nabla \cdot \bar{B} = 0 \quad (3)$$

Where,

\bar{E} : electric field strength vector (V/m).

q : electric charge density (C/m³).

\bar{B} : magnetic flux density vector (T).

\bar{J} : electric current density vector (A/m²).

\bar{D} : electric displacement vector (C/m²).

t : time (s).

\bar{H} : magnetic field intensity (A/m)

Constitutive relationships are the means of describing a material's response to EM fields. For GPR, the electrical and magnetic properties are of importance. Constitutive equations (equations 4, 5, and 6) provide a macroscopic description of how electrons, atoms, and molecules respond to the application

of an EM field.

$$\bar{J} = \tilde{\sigma} \bar{E} \quad (4)$$

$$\bar{D} = \tilde{\epsilon} \bar{E} \quad (5)$$

$$\bar{B} = \tilde{\mu} \bar{H} \quad (6)$$

Where,

$\tilde{\sigma}$: electrical conductivity that characterizes free charge movement (creating electric current) when an electric field is present.

$\tilde{\epsilon}$: dielectric permittivity that characterizes displacement of charge constrained in a material structure to the presence of an electric field.

$\tilde{\mu}$: magnetic permeability, which describes how intrinsic atomic and molecular magnetic moments respond to a magnetic field.

$\tilde{\sigma}$, $\tilde{\epsilon}$, and $\tilde{\mu}$ are tensor quantities and can also be nonlinear, i.e., $\tilde{\sigma} = \tilde{\sigma}(\mathbf{E})$. For most GPR applications, assuming the scalar constant form for σ , ϵ , and μ suffices, with ϵ and σ being the most important.

In most GPR applications, variations in ϵ and σ are most important, while variations in μ are seldom of concern. GPR is most useful in low-electrical-loss materials. If $\sigma = 0$, GPR would see extensive use since signals would penetrate to great depth. In practice, however, low-electrical-loss conditions are not prevalent.

Earth materials are invariably compositing many other materials or components. Water and ice represent the few cases where a single component is primarily present. Simple beach sand is a mixture of soil grains, air, water, and ions dissolved in water. Soil grains will typically occupy 60–80 percent of the available volume.

Understanding the physical properties of mixtures is, thus, a critical factor in the interpretation of a

GPR response. Combinations of materials seldom exhibit properties directly in proportion to the volume fraction of the constituent components. In many respects, this complexity can make a quantitative analysis of GPR data impossible without ancillary information.

Fundamental wave field properties are velocity (v), attenuation (α), and EM impedance (Z). Wave properties for a simple medium with fixed permittivity, conductivity, and permeability are most easily expressed if a sinusoidal time variation is assumed, for the interpretation of n and f versus sinusoidal frequency, f (note $\omega = 2\pi f$).

All the wave properties exhibit similar behavior. At low frequencies, wave properties depend on radial frequency root ($\sqrt{\omega}$) which is indicative of diffusive field behavior. At high frequencies, the properties become frequency-independent (if σ , ϵ , and μ are frequency-independent). The high-frequency behavior is the characteristic of most importance to GPR.

GPR systems are conceptually simple; the objective is to measure field amplitude versus time after excitation. The heart of a GPR system is the timing unit, which controls the generation and detection of signals.

The objective of reflection surveys is to map subsurface reflectivity versus spatial position. Variations in reflection amplitude and time delay indicate variations in v , α , and Z . GPR reflection surveys are traditionally conducted on “straight” survey lines, and systems are designed to operate in this fashion.

But simply, permittivity describes the ability of a material to store and release EM energy in the form of electric charge and classically relates to capacitors’ storage ability. Alternatively, it can be described as the ability to restrict the flow of free charges, or the degree of polarization (in F/m) exhibited by a material under the influence of an applied electric field. It is usually quoted in terms of a nondimensional, relative permittivity term (ϵ_r).

$$\epsilon_r = \frac{\text{permittivity of material } (\epsilon)}{\text{permittivity of free space or vacuum } (\epsilon_o)} \quad (7)$$

The permittivity of free space (or permittivity constant) is given as 8.8542×10^{-12} F/m, and differs negligibly from air permittivity. In some older texts, the relative permittivity of a material is sometimes referred to as the ‘dielectric constant’, and given the symbol κ , though this practice is less common now.

The permittivity of subsurface materials can vary dramatically, especially in the presence of free and bound water, and is usually a complex, frequency-dependent quantity with real (storage) and imaginary (loss) components. The permittivity value of a material is often simplified to its constant, low-frequency (or static) real component with the loss term ignored. This is convenient for the approximate calculation of radar wave velocities and wavelengths but is too general for a detailed analysis.

The primary material property obtained from GPR surveys is the dielectric constant. The dielectric constant, also known as the relative permittivity (ϵ_r) of a homogeneous media relates the relative EM velocity (v) in a material to the speed of light in free space, c ⁽²⁶⁾:

$$\epsilon_r = \left(\frac{c}{v}\right)^2 \quad (8)$$

The formulations are of more use, practically, and determine the effective permittivity of a mixture from a knowledge of its component parts. In general, these models assume that the material is a multi-phase mixture of geometrically simple shapes or inclusions in a matrix (e.g., solid spheres in a fluid) or a composite of uniform layers. There is a range of applicable formulations:

- Complex refractive index model (CRIM).
- Maxwell–Garnet theory (MGT).

- Effective medium theory (EMT).
- Looyenga model.
- Hanai–Bruggeman and Bruggeman–Hanai–Sen (BHS) models.

Of these, the CRIM, plus its derivatives, and the BHS model, have become the most popular for GPR-based hydrological/contaminant applications because they are simple to apply, robust, and accurate over the GPR frequency range.

The CRIM model is strictly a one-dimensional, layered medium model and has been shown to be effective for medium- to coarse-grained, multi-phase mixtures involving simple granular materials (e.g., semi-spherical sand grains) and moderate- to low-viscosity fluids.

It has the advantage of being a volumetric model that requires only knowledge of the materials' permittivity and their fractional volume percentages and can be used on both the real and imaginary components of the complex permittivity. In its general form, the CRIM formula is written as follows:

$$\epsilon_{\text{mix}}^e = \left(\sum_{i=1}^N f \sqrt{\epsilon_i} \right)^2 \quad (9)$$

Where,

ϵ_{mix}^e : complex bulk effective permittivity of the mixture.

f : volume fraction of the i^{th} component.

ϵ_i : complex permittivity of the i^{th} component.

Saarenketo ⁽²⁷⁾ is one of the first researchers in Europe to use GPR to measure asphalt pavement density. His study was based on the concept that the dielectric constant of pavement can be assumed to be a function of the dielectric constants of its components.

Therefore, changes in the pavement system proportions (e.g., void content) can be measured by recording the overall dielectric constants of the pavement. The components of the asphalt mixture

include asphalt, aggregate, air, and possible water. The dielectric constants for asphalt usually remain in the range of 2.6 to 2.8, those for crushed dry aggregate vary between 4.5 and 6.5, and those for air stand at 1.

Based on the EM mixing theory, three hot-mix asphalt (HMA) bulk specific gravity models were developed, and the ability of GPR to predict in-place HMA density was investigated ⁽²⁸⁾. The best model was selected through laboratory testing and validated by field testing.

Estimated HMA dielectric constant from GPR can yield the pavement's density and air void content when an appropriate model is used ^(29, 30). When GPR is used for in-place HMA pavement density prediction, the density profile of the entire pavement can be obtained. This significantly improves the reliability of the in-situ pavement density prediction, considering that all the other in-place density measurement methods can provide density data only at discrete sampling locations.

Soil is a composite material that consists of solid particles, air, and water. The density of soil depends on the specific gravities and volumetric fractions of its components. In a similar way, the dielectric constant of the soil is a function of the dielectric and volumetric properties of its components, as previously mentioned. Various EM mixing models are available to predict the dielectric constant of a mixture based on the dielectric constants and volume fractions of its components. Most of these models hypothesize that a mixture is composed of a background material with inclusions of different sizes and shapes.

The initial objective of this research is to develop a model that can be used to predict subgrade soil dry density, based on its dielectric constant using these EM mixing formulas along with connecting the subsurface condition with the surface conditions captured from surface cameras to fully understand and evaluate the pavement condition.

GPR Interpolations

The most important factors in determining a soil's dielectric permittivity are porosity and water saturation. Air has a relative permittivity of 1.0, whereas common soil-forming minerals have much higher relative permittivity. This means that for dry samples, the soil's bulk dielectric permittivity decreases as the porosity increases. Figure 4 shows a schematic diagram of the reflections of a GPR signal from a layered pavement system.

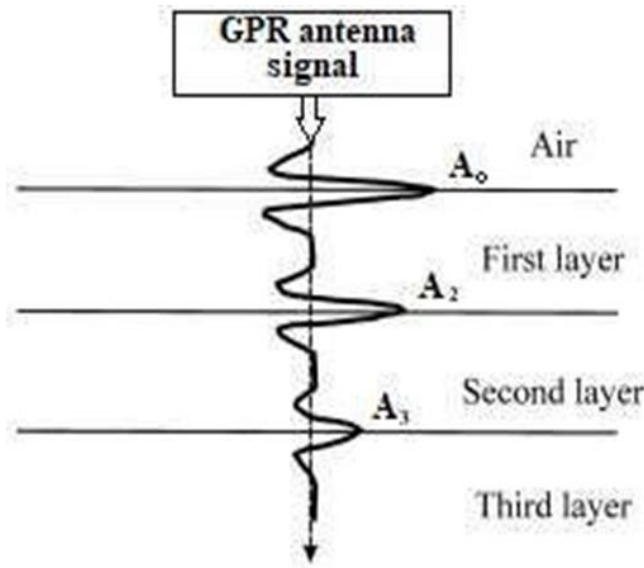


Figure 4. Chart. Multi layered system diagram of GPR signal reflection.

The dielectric values of the asphalt concrete (first layer) and the base layers (ϵ_1 , and ϵ_{Base}) can be computed using equations 10 and 11, respectively.

$$\epsilon_1 = \left(\frac{1 + \frac{A_0}{A_m}}{1 - \frac{A_0}{A_m}} \right)^2 \quad (10)$$

$$\epsilon_{Base} = \epsilon_{HMA} \left(\frac{1 - \left(\frac{A_0}{A_m} \right)^2 + \left(\frac{A_{Base}}{A_m} \right)^2}{1 + \left(\frac{A_0}{A_m} \right)^2 - \left(\frac{A_{Base}}{A_m} \right)^2} \right)^2 \quad (11)$$

Where,

ϵ_{HMA} : dielectric constant for the HMA layer.

A_o : amplitude of the surface reflection.

A_m : amplitude of the reflected signal collected over a metal plate placed on the surface.

A_{base} : amplitude of the reflected signal collected over the subbase layer surface.

The dielectric value ϵ_n for the third layer onward (n^{th} layer) can be evaluated as equation 12, where γ_i is the reflection coefficient at the i^{th} layer interface calculated from equation 13.

$$\epsilon_{r,n} = \epsilon_{r,n-1} \left(\frac{1 - \left(\frac{A_o}{A_m}\right)^2 + \sum_{i=1}^{n-2} \gamma_i \left(\frac{A_i}{A_m}\right) + \left(\frac{A_n}{A_m}\right)}{1 - \left(\frac{A_o}{A_m}\right)^2 + \sum_{i=1}^{n-2} \gamma_i \left(\frac{A_i}{A_m}\right) - \left(\frac{A_n}{A_m}\right)} \right)^2 \quad n > 2 \quad (12)$$

$$\gamma_i = \frac{\sqrt{\epsilon_{r,i}} - \sqrt{\epsilon_{r,i+1}}}{\sqrt{\epsilon_{r,i}} + \sqrt{\epsilon_{r,i+1}}} \quad (13)$$

Often a single calibration value (for determining material properties such as depth) is used for large amounts of collected GPR data, but currently, there is little study of how the calibration maybe affected by variation in material properties. This variability implies that data calibration procedures may need to be altered to maintain the robustness of the information determined from GPR data.

CHAPTER 3. MODEL DERIVATION AND IMPLEMENTATION

The density and deformation properties of soils and aggregates are mostly affected by interparticle voids, which exert outstanding effects on the bearing ratio of unbound materials in airfields and road pavements. Considering that the physical characteristics of soils depend on voids between particles and assuming that dielectric properties of materials are related to density, a reasonably good correlation between dielectric and physical properties of soils would be expected. Based on this idea, further research on dielectric properties and soil physical properties of subgrade soil material is followed.

OBJECTIVE

In this chapter, the possibility to infer the physical characteristics of unbound compacted subgrade soils from their dielectric properties through GPR is investigated. Specifically, this study is aimed at providing a GPR-based approach for an effective and efficient pavement assessment model. The proposed model was calibrated through laboratory tests conducted under controlled compaction conditions and validated by using in situ density measurements collected on soils in Georgia.

THEORETICAL BACKGROUND

Overall, two main approaches are followed, relying on, respectively: (1) the potential dependence between dielectric constant and density of subgrade soils, and (2) the dependence of empirical equations for road pavement design on the bulk stress state within the pavement layer. A semi-empirical model is proposed by exploiting the common dependence of such two approaches on deformation properties of subgrade soils.

Dielectric constants of materials were estimated according to the EM theory's fundamentals that were

described in chapter 2. Regarding the processing of GPR data, permittivity estimates of the soil were carried out using surface reflection techniques.

DENSITY PREDICTION MODEL

In accordance with the CRIM mixture theory, the dielectric constant of a homogenous mixture can be estimated by the “power-law” approximation. A widely used class of mixing models is shown in equation 14.

$$\epsilon_{\text{eff}}^{\beta} = f \epsilon_i^{\beta} + (1 - f) \epsilon_e^{\beta} \quad (14)$$

In this model, a certain power of the permittivity is averaged by volume weights. f is the volume fraction and b is a constant dependent on the mixture’s composition and is assumed to be 0.5 ⁽³¹⁾. Assuming the total volume of soils phases is assumed as 1, equation 14 can be rewritten as equation 15.

$$\epsilon_{\text{soil}}^{\beta} = V_a \cdot \epsilon_a^{\beta} + V_w \cdot \epsilon_w^{\beta} + V_s \cdot \epsilon_s^{\beta} \quad (15)$$

Based on the previously mentioned empirical assumptions that dielectric constants are indirectly related to physical characteristics of soils, a semi-empirical model is suggested to predict the dry density and water content of subsurface layers from their relative permittivity, ϵ_{soil} . Using equation 15 and the soil phase diagram (figure 5), equation 17 is derived as follows:

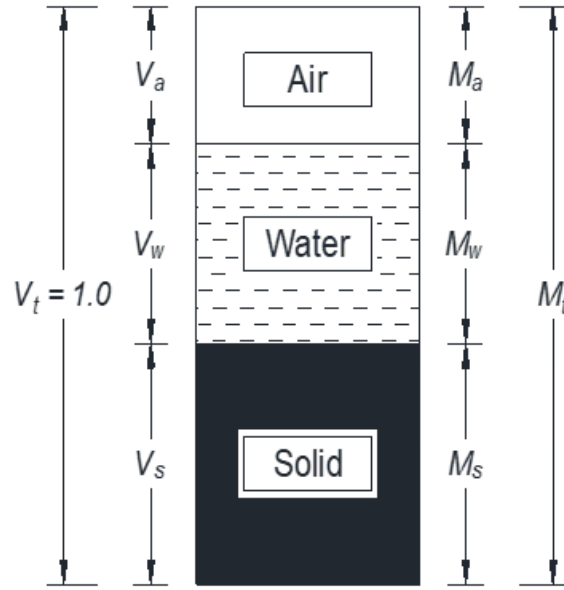


Figure 5. Chart. Soil phase diagram.

Where,

V_a : air voids volume in soil

M_a : air voids mass = 0

V_w : water volume in soil

M_w : mass of water

V_c : solid particles volume in soil

M_c : mass of solids

ϵ_{soil} : soil media dielectric constant

ϵ_a : air dielectric constant = 1.0

ϵ_w : water dielectric constant = 80–81

ϵ_c : soil particles dielectric constant

From phase diagram relations, assuming $V_t = 1.0$,

$$\therefore \gamma_d = \frac{GS \cdot \gamma_w \cdot (1 - \frac{V_a}{V_t})}{1 + w \cdot GS} = \frac{GS \cdot \gamma_w \cdot (1 - V_a)}{1 + w \cdot GS}, \therefore V_a = 1 - \frac{\gamma_d \cdot (1 + w \cdot GS)}{GS} \text{ ----- (i)}$$

$$\therefore \gamma_d = \frac{M_s}{V_t} = M_s, \therefore \gamma_d = M_s \text{ ----- (ii)}$$

$$V_w = w \cdot M_s \text{ ----- (iii)}, V_s = \frac{M_s}{GS} \text{ ----- (iv)}$$

$$\epsilon_{\text{soil}}^{0.5} = V_a \cdot \epsilon_a^{\frac{1+\alpha}{\alpha}} + V_w \cdot \epsilon_w^{0.5} + V_s \cdot \epsilon_s^{0.5} \text{ ----- (v)}$$

Substituting i, ii, iii, and iv in v, we arrive at equation (16).

$$\begin{aligned}
\therefore \sqrt{\epsilon_{soil}} &= 1 - \frac{\gamma_d \cdot (1 + w \cdot GS)}{GS} + w \cdot \gamma_d \cdot \sqrt{\epsilon_w} + \frac{\gamma_d}{GS} \cdot \sqrt{\epsilon_s} \\
\therefore \sqrt{\epsilon_{soil}} - 1 &= \gamma_d \cdot \left[-\frac{1}{GS} - w + w \cdot \sqrt{\epsilon_w} + \frac{1}{GS} \cdot \sqrt{\epsilon_s} \right] \\
\therefore \sqrt{\epsilon_{soil}} - 1 &= \gamma_d \cdot \left[\frac{1}{GS} (\sqrt{\epsilon_s} - 1) + w (\sqrt{\epsilon_w} - 1) \right] \\
\therefore \gamma_d &= \frac{(\sqrt{\epsilon_{soil}} - 1)}{\frac{1}{GS} (\sqrt{\epsilon_s} - 1) + w (\sqrt{\epsilon_w} - 1)} \quad (16)
\end{aligned}$$

Relationship between water content & permittivity

The most used relationship between apparent permittivity, ϵ , and volumetric soil water content, θ (m^3/m^3), was proposed by Topp et al.⁽²⁶⁾.

$$\theta = -0.053 + 0.0292 (\epsilon_{soil}) - 5.5 \times 10^{-4} (\epsilon_{soil})^2 + 4.3 \times 10^{-6} (\epsilon_{soil})^3, \quad (17)$$

Equation 17 was determined empirically for mineral soils having various textures. The term ‘apparent’ is used because the permittivity used in this equation is determined from the measured electromagnetic propagation velocity in the soil. The water content of the soil is then calculated from volumetric water content as shown in equation 18.

$$w = \theta / \gamma_{soil} \quad (18)$$

MODEL IMPLEMENTATION

Using equations 16 and 17, the subgrade soils’ dry density can be calculated with an assumed gravimetric water content (w). Volumetric water content (θ) calculation is performed through equation 17. According to the AASHTO⁽³²⁾, the equation calculates the gravimetric water content

(w) followed by the error between the calculated and estimated gravimetric content. Generalized Reduced Gradient (GRG) within the Microsoft Excel Solver is used to minimize the error and recalculate the correct values for estimated and calculated gravimetric water content as shown in figure 6.

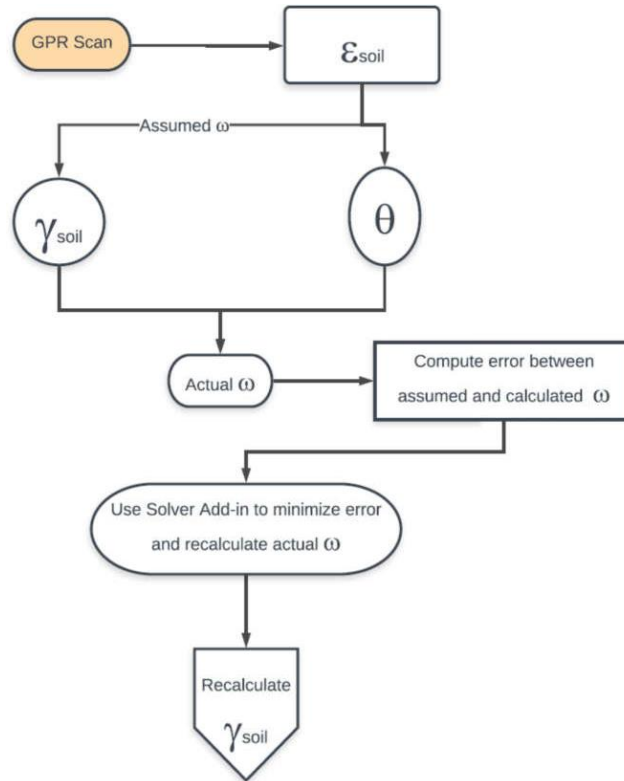


Figure 6. Chart. GPR–dry density model implementation

MODEL CALIBRATION

The subgrade density model described in equation 16 was calibrated by a series of laboratory test results. Details of the model calibration are illustrated in chapter 4.

CHAPTER 4. MODEL VALIDATION FOR SUBGRADE DENSITY

LABORATORY TEST

A set of laboratory tests were conducted to build the database to prove our proposed method in establishing the relationship between GPR scanning results and subgrade soil physical properties.

The laboratory testing program took place at the University of Georgia's (UGA) Geomaterials Research Lab in Athens, Georgia. A problematic high plastic silt soil readily found in North Georgia was used as the subgrade material. Test specimens were prepared in a large metal box measuring 2 m long \times 2 m wide \times 0.7 m deep (6 ft long \times 6 ft wide \times 2 ft deep), as shown in figure 7 and figure 8. Each sample measures 1.0 m long \times 0.7 m wide. The soil and water were mixed till reaching the desired water content for soil compaction. The soil was then transported to the steel box and gradually compacted using a vibrating table. GPR surveys were carried out for each compaction step up to the maximum density available, as shown in figure 7. Subgrade soil specimens were constructed with 0.3 m (12 inches) in depth and compacted to reach six different density levels, as shown in figure 8.



Figure 7. Photos. Sample preparation photos: (a) Soil transportation and filling testing box, (b) soil compaction



Figure 8. Photo. divided soil samples.

Physical Properties Testing

The physical properties of the soils were measured to compare the properties derived from the GPR scan results.

Grain size Distribution

The soil was classified as high plasticity silt (MH) per the Unified Soil Classification System (USCS) and A-7-5 according to the AASHTO ⁽³²⁾ classification system.

Specific Gravity

The specific gravity of the tested soil was calculated based on ASTM D854-14. The specific gravity value is vital for GPR–density model calculations. The soil index properties for these soils are provided in table 1.

Table 1. Soil specimen index properties.

Specific Gravity	USCS Classification	Fines (%)	PL	LL	PI
2.76	MH	57.21	37.44	57.1	19.7

Maximum Dry Density

The maximum dry density for the soil sample was measured in accordance with ASTM standard

D1557. The soil maximum dry density was found to be 116.75 pcf (1.871 t/m³) with optimum water content of 24.6 percent.

Laboratory Sand Cone Test

After the specimens were prepared, the bulk density of each specimen was measured using sand cone tests, as shown in figure 9. The results of the sand cone tests are illustrated in table 2.



Figure 9. Photo. laboratory sand cone test.

Table 2. Laboratory sand cone test results.

Sample	Bulk Density (γ_{bulk})		Water Content %	Dry Density (γ_{dry})	
	(t/m ³)	(pcf)		(t/m ³)	(pcf)
D1	1.951	121.8	22.49	1.593	99.4
D2	2.119	132.3	21.05	1.750	109.3
D3	1.759	109.8	20.43	1.461	91.2
D4	2.321	144.9	24.43	1.865	116.4
D5	2.090	130.5	26.60	1.651	103.1
D6	1.603	100.1	18.69	1.351	84.3

It should be noted that specimens D1 through D5 were compacted with varying compaction efforts, while D6 was not compacted at all. Therefore, it is believed that the D6 specimen had a higher void ratio compared to the other specimens.

GPR Calibration

After the sand cone tests were conducted, GPR data were collected from six samples using a 2.0 GHz air-coupled antenna, as shown in figure 10. The data acquisition system was calibrated before each scan to validate the signals with a perfect reflection on a metal plate. This calibration also provided some preliminary data for the processing, with A_m (amplitude of the reflected wave on the metal plate to estimate the dielectric constants for the subsequent layers) to calculate the density and water content ratios for the targeted samples by the GPR scan.



Figure 10. Photo. GPR Scanning and calibration for different samples.

The calibration of the GPR system was performed with a metal plate on top of the soil specimen. From this calibration process, A_m was found to be 7,942,173, as shown in figure 11. Figure 12 shows the amplitude of the surface reflection measured from each soil specimen. Using the measured amplitude values from GPR, the dielectric constants for the six soil specimens were calculated using equation 10. Table 3 summarizes the calculated dielectric constant for each specimen.

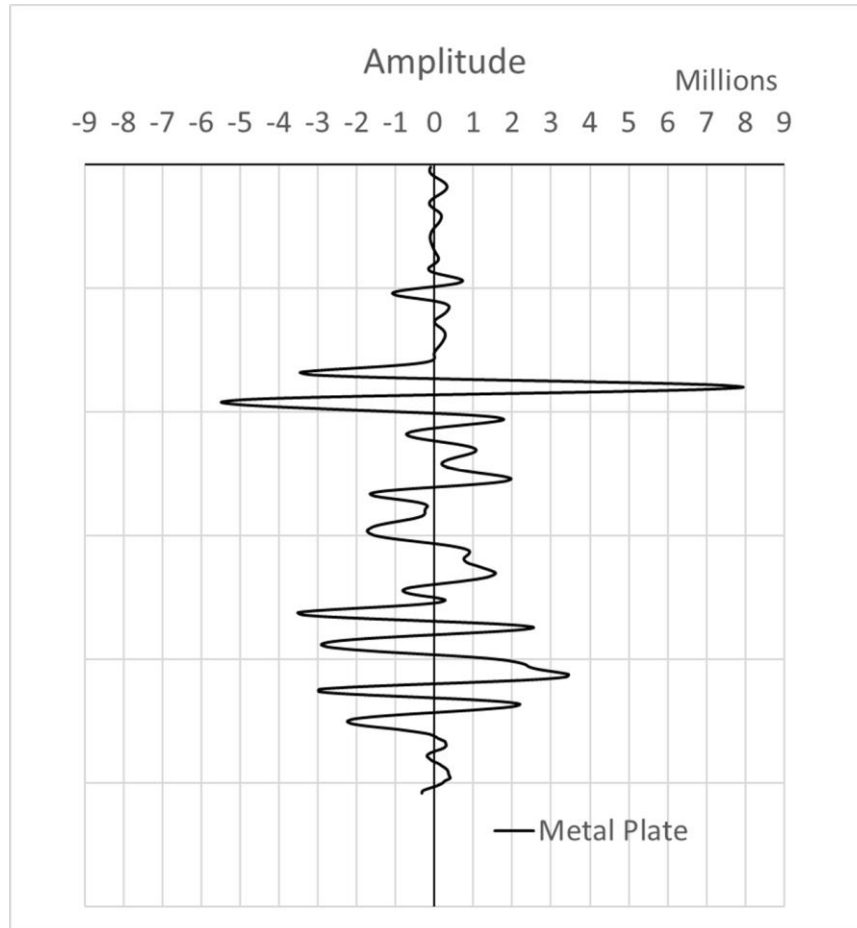


Figure 11. Graph. Amplitude from metal plate calibration.

Table 3. Dielectric constant results.

Sample ID	Amplitude	ϵ
D1	5,257,634	24.18
D2	5,318,661	25.55
D3	4,827,136	16.80
D4	5,788,944	40.67
D5	5,740,596	38.63
D6	3,378,338	6.15

Laboratory GPR Scan Results

Table 4 shows the results for the GPR–density model implementation. Figure 12 also shows the amplitude of the surface reflection measured from each soil specimen.

Table 4. Proposed model calculation results.

Sample ID	w % Measured	γ_{dry} Initial		θ	w % Calculated	γ_{dry} Calculated	
		t/m ³	pcf			t/m ³	pcf
D1	22.5%	1.977	123.4	39%	17%	1.644	102.6
D2	21.1%	2.047	127.8	41%	17%	1.702	106.2
D3	20.4%	1.564	97.7	30%	17%	1.301	81.2
D4	24.4%	2.714	169.4	51%	16%	2.257	140.9
D5	26.6%	2.632	164.3	50%	16%	2.189	136.7
D6	18.7%	0.747	46.7	11%	13%	0.621	38.8

Note: $\epsilon_{\text{water}} = 80$ (80–81), $\epsilon_{\text{soil}} = 15$ (5–30)

Table 5 shows the calculated bulk density from the model and measured bulk density from the sand cone tests. Generally, the percent error ranged from 3 to 24 percent. A substantial error with 118 percent was observed for the specimen with the lowest density. Figure 13 shows the comparison of measured and calculated bulk densities along with the line of equality.

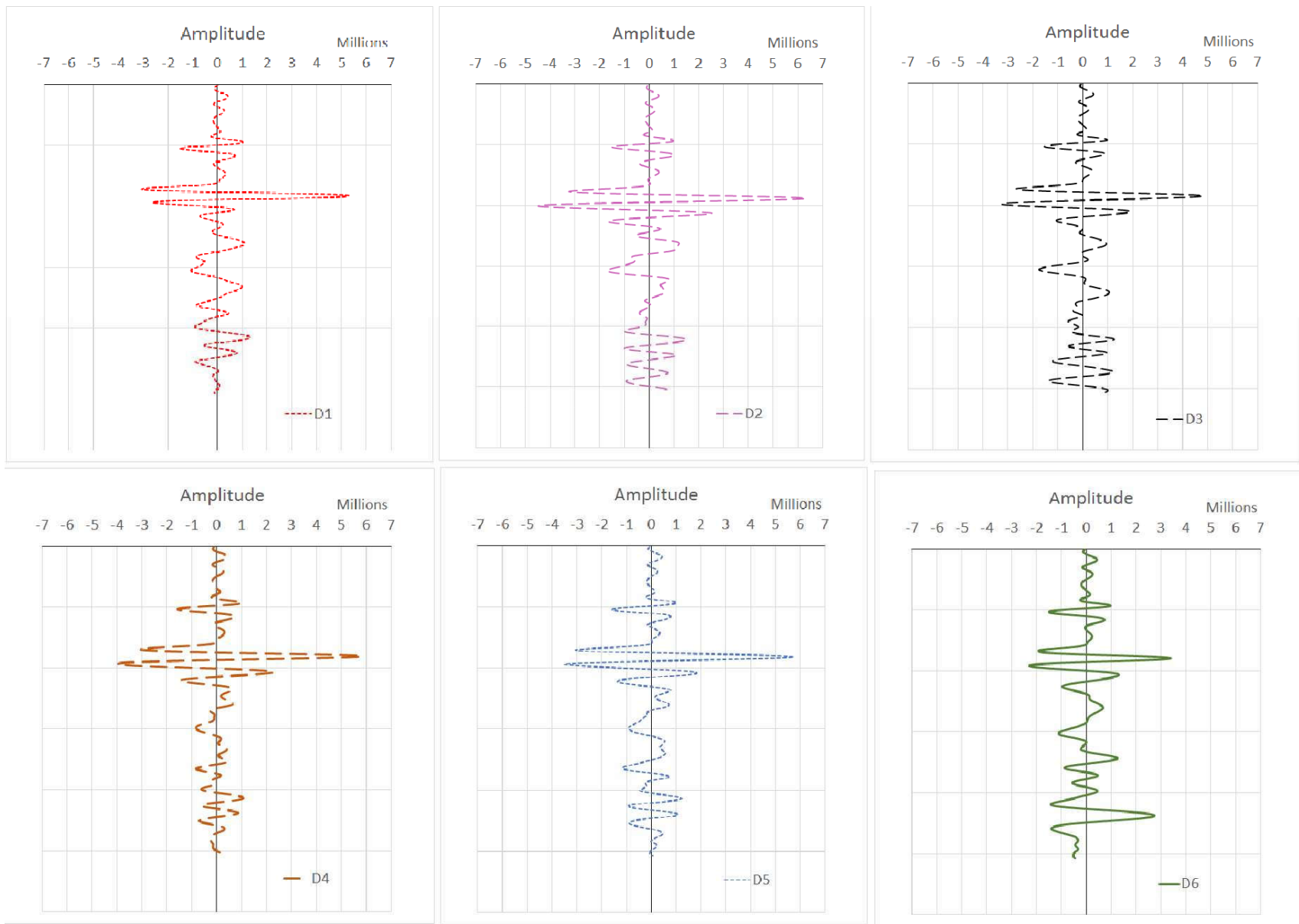


Figure 12. Graphs. Amplitude for different soil samples.

Table 5. Comparison between proposed model and sand cone test results.

Sample ID	γ_{dry} Calc.		Dry Density (Sand Cone Test)		Error %
	t/m ³	pcf	t/m ³	pcf	
D1	1.637	102.2	1.593	99.4	3%
D2	1.695	105.8	1.750	109.3	3%
D3	1.295	80.9	1.461	91.2	13%
D4	2.247	140.3	1.865	116.4	17%
D5	2.180	136.1	1.651	103.1	24%
D6	0.619	38.6	1.351	84.3	118%

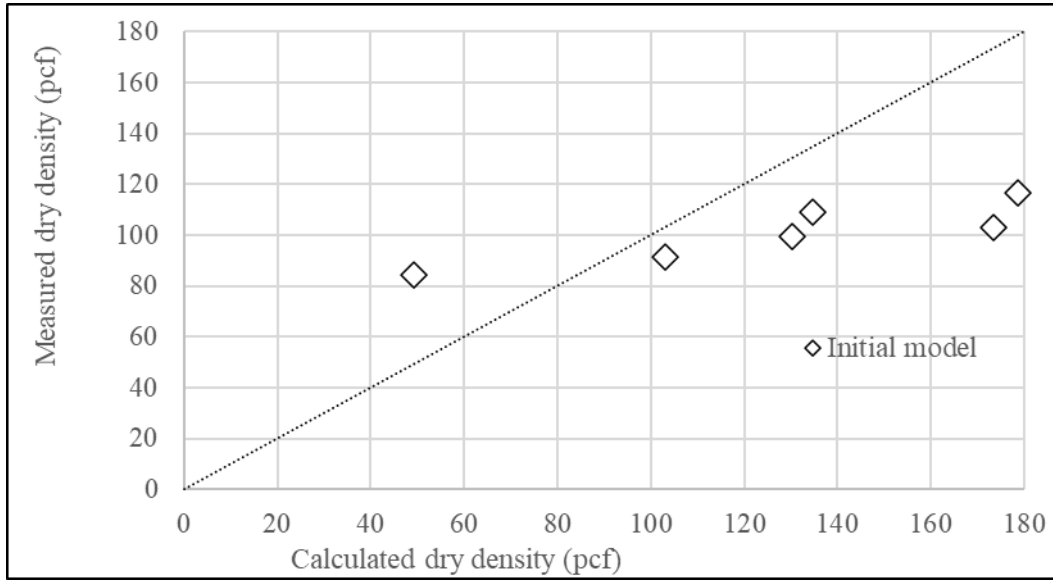


Figure 13. Graph. Comparison between measured and calculated soil dry densities.

Abdelmawla and Kim⁽³³⁾ proposed a model that measured density should be validated with a back calculated value to reflect the soil physical properties in the field. To adjust the error between the calculated and measured bulk density, an exponential model was utilized, as shown in equation 19.

$$\gamma_{\text{dry, estimated}} = \alpha (\gamma_{\text{dry, calculated}})^{\beta} \quad (19)$$

Based on the laboratory tests, the fitting coefficients of a and b were estimated as 1.464 and 0.171, respectively. It should be noted that these fitting coefficients were developed for highly plastic silt soils and should be used with caution for other soil types. The comparisons of measured and calculated subgrade density are shown in table 6 and figure 14. The subgrade soils' dry density estimated by the new exponential model shows approximately 11 percent maximum error compared to the soil's density measured by the sand cone method.

Table 6. Exponential model results.

Sample ID	γ_{dry} Measured		γ_{dry} Calculated with fitting coefficients		% Error
	t/m ³	pcf	t/m ³	pcf	
D1	1.593	99.4	1.593	99.4	0%
D2	1.750	109.3	1.602	100.0	9%
D3	1.461	91.2	1.531	95.6	5%
D4	1.865	116.4	1.681	104.9	11%
D5	1.651	103.1	1.672	104.4	1%
D6	1.351	84.3	1.351	84.3	0%

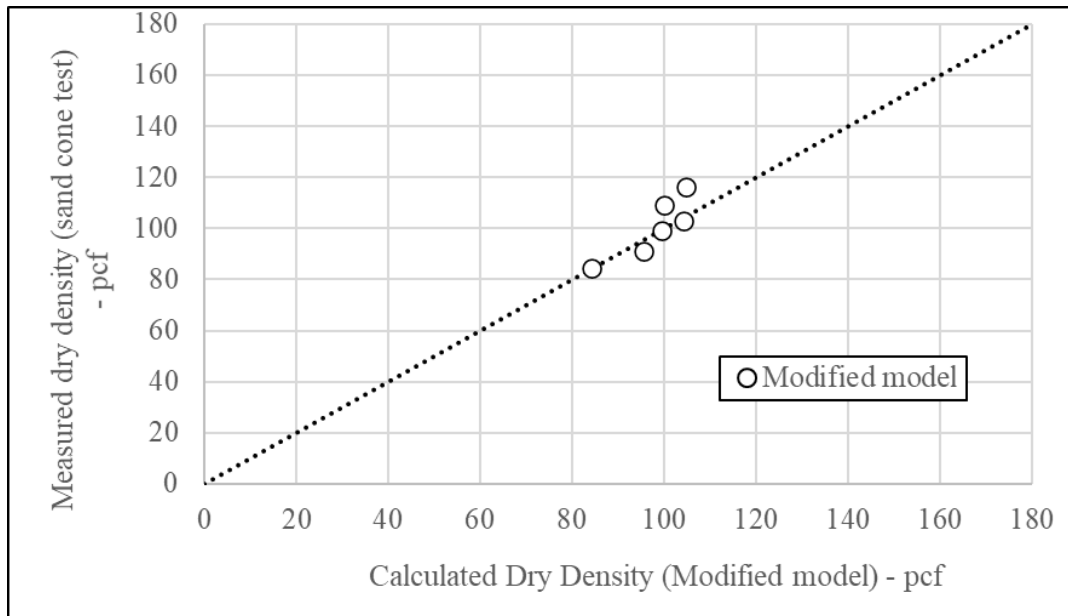


Figure 14. Graph. Exponential model vs measured soil bulk density.

FIELD VALIDATION

Field tests were conducted to validate the GPR–density model. Three sites were selected in the state of Georgia. Details of these locations on State Route (SR) 53, West Winder Pass, and SR 316 are shown in table 7 and depicted in figure 15, figure 16, and figure 17.

Table 7. Verification field tests.

Site	Location				Length (ft)
	Start		End		
SR 53	34.417658	−84.304409	34.4175185	−84.3054911	352.57
West Winder Pass	33.989741	−83.7787341	33.9912852	−83.7782494	626.52
SR 316	33.945245	−83.7518097	33.9447035	−83.7508741	350.1

SR 53



Figure 15. Photo. Field verification test 1 aerial photo.

West Winder Pass

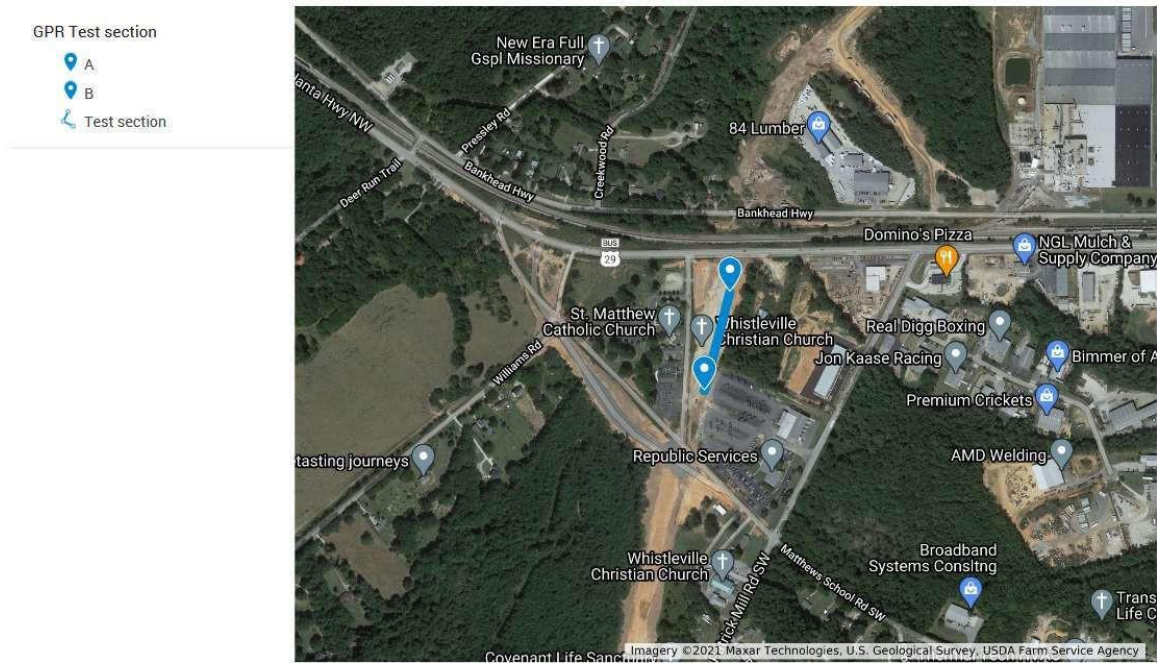


Figure 16. Photo. Field verification test 2 aerial photo.

SR 316

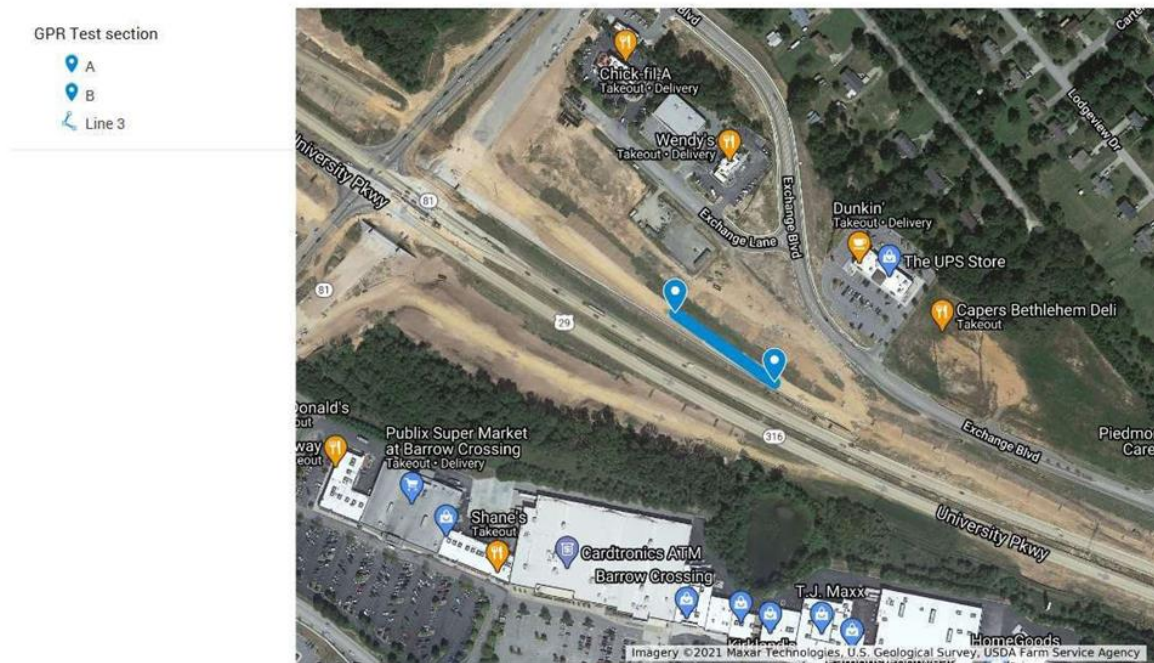


Figure 17. Photo. Field verification test 3 aerial photo.

GPR tests were carried out along two lines of scan across the lane width. The procedure was validated through sand cone tests to obtain field bulk density, dry density, and water content as shown in figure 18; results are shown in table 8, table 9, and table 10 for the three field test sites, respectively.



Figure 18. Photo. Sand cone test for SR 53 test section.

Table 8. SR 53 sand cone test results.

Sample	Bulk Density (γ_{bulk})		Dry Density (γ_{dry})		Water Content
	(t/m ³)	(pcf)	(t/m ³)	(pcf)	
S1	1.925	120.2	1.823	113.8	5.6%
S2	2.045	127.7	1.934	120.7	5.7%

Table 9. West Winder Pass sand cone test results.

Sample	Bulk Density (γ_{bulk})		Dry Density (γ_{dry})		Water Content
	(t/m ³)	(pcf)	(t/m ³)	(pcf)	
S1	2.162	135.0	1.729	107.9	23.7%
S2	2.005	125.2	1.635	102.1	19.9%
S3	2.087	130.3	1.696	105.9	24.2%

Table 10. SR 316 sand cone test results.

Sample	Bulk Density (γ_{bulk})		Dry Density (γ_{dry})		Water Content
	(t/m ³)	(pcf)	(t/m ³)	(pcf)	
S1	2.018	126.0	1.833	114.4	10.1%
S2	1.936	120.9	1.764	110.1	9.8%

GPR Scanning

GPR frequency data were collected using the UGA GPR van; a GPR SIR-30 scan system was deployed with two different antennas at two different frequency levels, 2 GHz, and 400 MHz. The UGA GPR system installed in the van is custom built, as shown in figure 19 and figure 20.



Figure 19. Photo. UGA GPR van.



Figure 20. Photo. UGA GPR road survey control units.

Field Verification Test Results

SR 53

The SR 53 section was tested, and the model was used to estimate the dry density compared to the results of the sand cone test of the field samples. The maximum error in the estimated result was found to be 5 percent, as shown in table 11; the results for the density of the entire section is shown in figure 21.

Table 11. Sand cone test results for SR 53.

Distance	γ_d Meas.		γ_d Calc.		Error
ft	t/m ³	pcf	t/m ³	pcf	
20.00	1.823	113.8	1.928	120.3	5%
120.00	1.934	120.7	1.957	122.2	1%

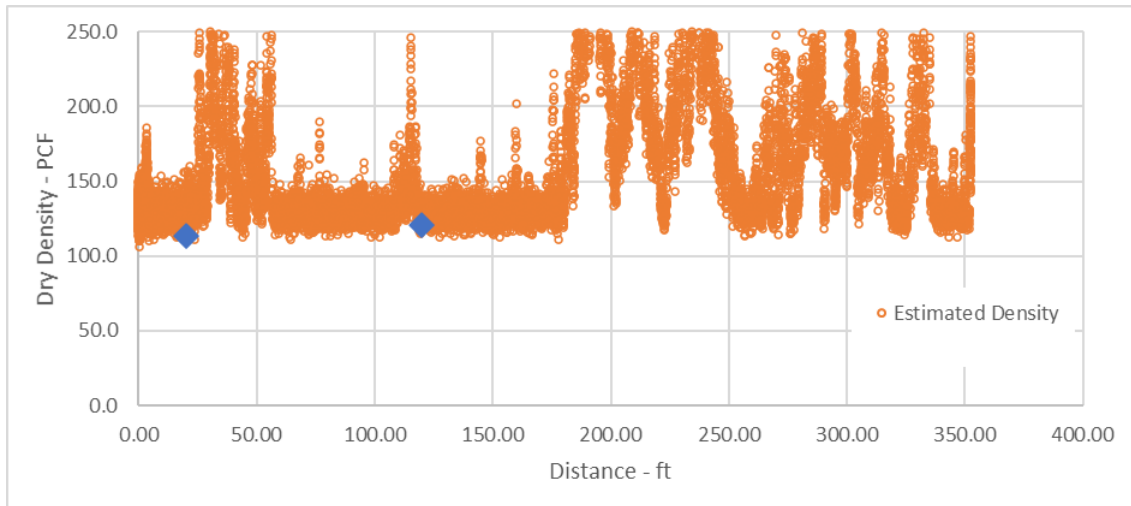


Figure 21. Graph. Calculated dry density for SR 53.

West Winder Pass

The error in the estimated result is shown in table 12. Also, the results for the estimated subgrade density of the entire section are shown in figure 22. Figure 23 shows the variation of estimated subgrade density along the travel distance, which indicates the locations where the strong and weak subgrade densities are suspected. It is inferred that the location where lower subgrade density is detected has a higher potential to show poor pavement performance with potential structural failure.

Table 12. Sand cone test results for West Winder Pass.

Distance	γ_d Meas.		γ_d Calc.		Error
ft	t/m ³	pcf	t/m ³	pcf	
350.00	1.833	114.4	1.8334	114.5	0.02%
300.00	1.764	110.1	1.7640	110.1	0.00%

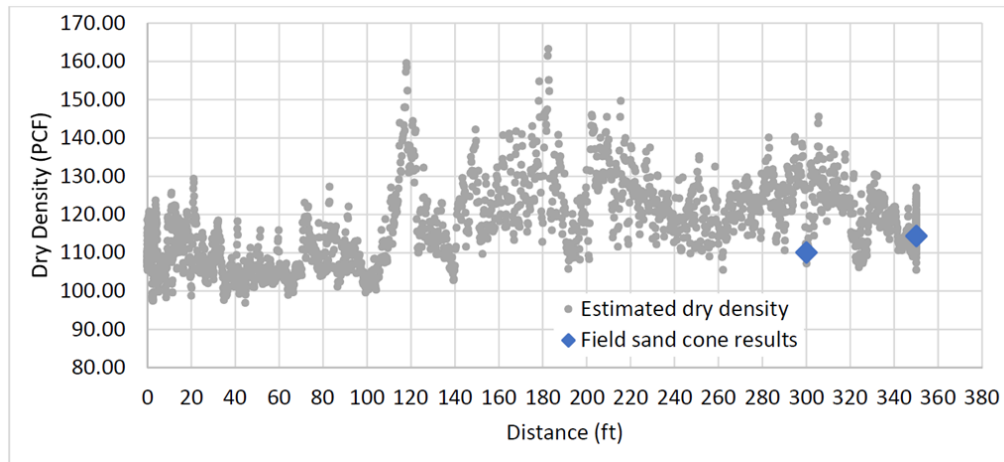


Figure 22. Graph. Calculated dry density for West Winder Pass.

SR 316

GPR test was also conducted for SR 316 as illustrated in chapter 3, and the proposed model was employed to estimate the subgrade dry density. The maximum error in the estimated result was found to be 2.67 percent, as shown in table 13; the results for the density of the entire section is shown in figure 23. According to the model validation study, it is concluded that the model performed well in estimating subgrade soil dry density for the tested locations. However, more field validations are recommended to investigate the effect of soil types on the model predictions.

Table 13. Sand cone test results for SR 316.

Distance	γ_d Meas.		γ_d Calc.		Error
ft	t/m ³	pcf	t/m ³	pcf	
300.00	1.729	107.9	1.7291	107.9	0.00%
400.00	1.635	102.1	1.6351	102.1	0.01%
500.00	1.696	105.9	1.6510	103.1	2.67%

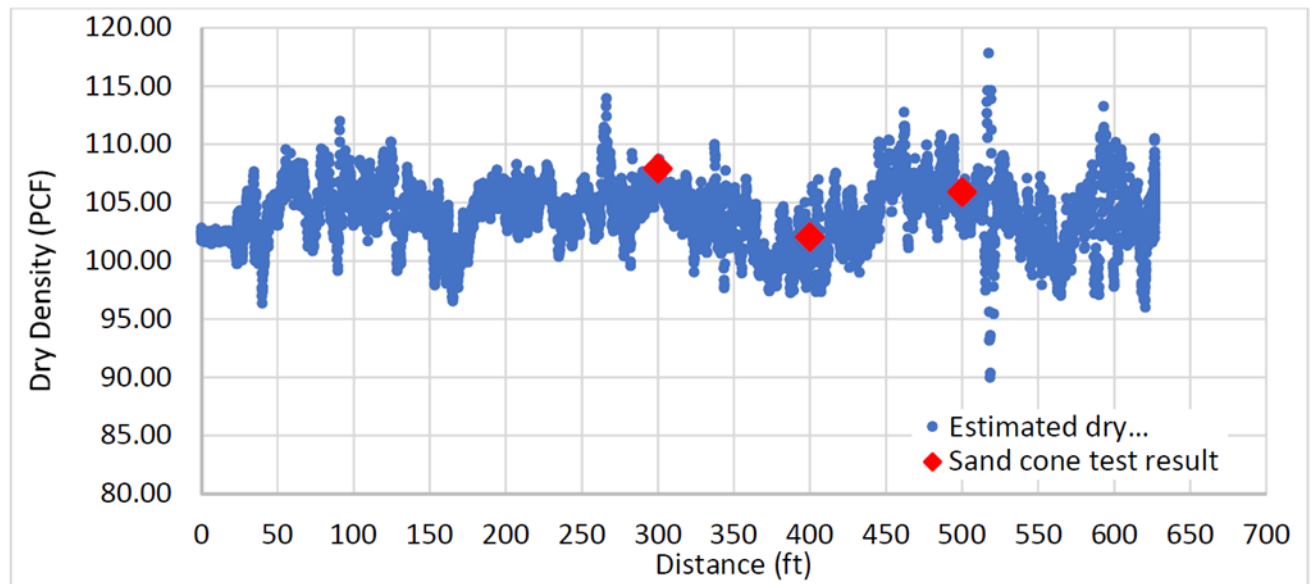


Figure 23. Graph of Calculated dry density for SR 316.

CHAPTER 5. RELATIONSHIP BETWEEN SUBGRADE DENSITY AND MODULUS FROM FALLING WEIGHT DEFLECTOMETER

INTRODUCTION

In this chapter, the developed GPR methodology is validated for the estimation of in situ subgrade modulus. For the validation, the GPR results for subgrade modulus along I-75 are compared to the values predicted by UGA-PAVE—falling weight deflectometer (FWD) back calculation software developed as part of Georgia Department of Transportation (GDOT) Research Project (RP) 18-05.

First, the chapter provides background on FWD back calculation methods in the context of the development of UGA-PAVE, followed by an overview of the UGA-PAVE software. Finally, the validation results are analyzed and discussed, and conclusions from the study are provided.

FWD BACK CALCULATION BACKGROUND

Pavement back calculation techniques are used to estimate the *in-situ* health of asphalt concrete pavements by inversely calculating parameters representing the dynamic modulus. The most common approach is to use a FWD ⁽³⁴⁾, which is a type of nondestructive testing equipment that rapidly impacts the pavement and measures the resulting displacement response on the surface. Deflection sensors are placed in a line extending from the point of loading to measure the displacement wave as it propagates through the pavement. FWD back calculation methods comprise two essential parts: an optimization scheme and a computational model of the pavement structure. In short, the optimization scheme uses the pavement model to identify a set of dynamic moduli which can most closely reproduce the experimentally measured deflections. The literature review presented here is separated into two sections—one concerning the advancement of numerical pavement models, and one pertaining to improvement of the optimization methodology.

Numerical Pavement Models

Despite the load imparted by the deflectometer being transient, the original FWD back calculation methods were static in nature. In static back calculation methods ^(35,36, 37), the numerical model only considers the deflection measurements at one time point to significantly reduce computational expense; however, static methods are prone to inaccuracies arising from the nonlinear nature of flexible pavements ^(38,39). Asphalt concrete is well known to be a viscoelastic material, meaning its strength varies nonlinearly with both temperature and the loading rate. Thus, multiple time points should be considered in the analysis to properly model the procedure.

Over time, dynamic FWD back calculation techniques have emerged ^(40, 41, 42, 39, 43, 44, 45), which offer improvements to accuracy by employing numerical models that consider the deflection response across multiple time points. The pavement models are commonly built using the finite element method (FEM) ^(35,36,38). A notable issue when modeling dynamic pavement responses via FEM is that significant errors arise due to wave reflection at the edges of the model. Traditionally, wave reflection has been addressed by increasing the size of the model until the reflections do not occur within the time frame of interest; however, the increased size usually leads to an exceptionally computationally expensive model ⁽³⁷⁾. Recent efforts have made considerable progress regarding wave reflection using methods such as perfectly matched layer ^(46, 47), enriched FEM ^(48, 49), and the layer transfer matrix method ^(50, 51, 51). However, each of these techniques has only been applied to the FWD back calculation problem with limited success.

An alternative numerical modeling approach is the spectral element method (SEM) originally devised by Rizzi and Doyle ^(53,54), which is essentially a derivative of FEM. Rather than using traditional finite elements built from polynomial shape functions, modern SEMs employ semi-infinite spectral

elements ^(55, 56, 57), constructed from harmonic functions that are more accurate for simulating wave propagation. The method uses discrete Fourier transform (DFT) to convert from the time domain and compute the solution in the frequency domain. Furthermore, SEMs require dramatically less computational resources than comparable finite element models because each layer of the pavement structure can be sufficiently modeled via a single spectral element. Furthermore, finite layer methods (FLMs) have been developed which are similar to SEM in that they use the DFT to solve the system of equations in the frequency domain ^(58, 41, 59). However, FLMs employ a different approach by computing the unit impulse response of the pavement structure, the response to the time domain, and then convolving the impulse response with the FWD load to calculate the surface deflections.

A notable drawback associated with SEM and FLM is the use of DFT to convert between the time and frequency domains. Time histories collected from FWDs are transient nonperiodic signals and are prone to measurement errors (e.g., noise). Furthermore, due to their viscoelastic nature, many harmonics are required to effectively model flexible pavements in the frequency domain, and it has been shown ⁽⁶⁰⁾ that DFT is not ideal for converting signals with such characteristics. Lee ^(61, 62) recently developed ViscoWave, an FLM that avoids the use of DFT by instead employing a combination of the Laplace and Hankel transformations.

ViscoWave combines the best characteristics of both FLM (i.e., efficient solution calculation through convolution of the FWD load and impulse response) and SEM (i.e., efficiently modeling each layer of the pavement with a single spectral element) into a single approach and is therefore the algorithm used in UGA-PAVE for the pavement modeling.

Optimization Routines

Despite the improvements discussed in the previous section, dynamic back calculation remains challenging due to various difficulties in the optimization ⁽³⁹⁾. The most troublesome issues with the optimization arise from the inverse nature of the problem. When the pavement is modeled with high accuracy, the back calculation becomes distinctly “ill-posed” ⁽⁶³⁾, primarily because the optimization must use a greater number of input variables (i.e., pavement layer moduli) than output variables (i.e., displacement sensor time histories), creating the likelihood of non-unique solutions ⁽⁶⁴⁾. In an FWD back calculation analysis, the ill-posedness manifests as multiple sets of dynamic moduli for which the model generates near-identical deflection time histories. The optimization also tends to be ill-conditioned due to the numerical model’s output varying in sensitivity among the moduli. Additionally, FWD measurements contain significant noise, and ill-conditioned systems are highly sensitive to such measurement error, further complicating the analysis.

A popular choice for optimizing the FWD back calculation is nonlinear least squares ^(65,37), which seeks to minimize the squared norm of the error between the measured and predicted dynamic deflections. Such problems are usually solved via Newton’s method; however, the classical Newton’s method tends to converge locally and exhibits poor performance when the initial guess is far from the global minimum ⁽⁶⁵⁾. Trust-region (TR) methods were developed to refine the convergence properties of Newton’s method and have improved nonlinear least squares optimization in a wide range of applications ^(67,68,69,70). A popular Newton-based method is the subspace trust-region interior reflective (STIR) algorithm ⁽⁷¹⁾ for its efficiency and reliability. The most notable aspect of the STIR method involves its subspace implementation. Original trust-region methods calculate the Newton step within the full-size Hilbert space (i.e., with dimensions equal to the number of updating variables). The STIR’s subspace modification limits the number of dimensions during computation to just two, thereby

reducing computational expense for little cost to accuracy.

Perhaps the most notable alternative to Newton-based TR methods is the Levenberg–Marquardt algorithm (LMA), which is essentially a Tikhonov-regularized Gauss–Newton algorithm (GNA) that operates similarly to a TR method. Because the objective function in the optimization is a sum of squares, it has unique properties that allow Newton’s method to be re-posed in a manner such that computation of second-order derivatives can be avoided. This is advantageous for problems consisting of many variables (e.g., 100 or more) or with computationally expensive second derivatives. The latter advantage is useful particularly for FWD back calculation because their second-order derivatives must be calculated using finite-difference approximations, which involve numerous costly function evaluations. Recently, Bellavia and Riccietti ⁽⁷²⁾, developed an LMA specifically tailored for solving ill-posed nonlinear least squares problems by modifying the Gauss–Newton algorithm to resemble the structure of Newton-based TR methods.

DESCRIPTION OF BACK CALCULATION SOFTWARE

UGA-PAVE is a dynamic FWD back calculation technique and comprises state-of-the-art computational methods for the forward model (i.e., simulates the FWD displacement response) and optimization routine (i.e., calculates the pavement layer moduli). For the forward model, UGA-PAVE employs the ViscoWave algorithm, and for the optimization the tandemtrust-region technique is used, which was developed as part of RP 18-05 and combines both the STIR and LMA techniques into a hybrid scheme.

The primary deliverable of UGA-PAVE is to estimate the dynamic modulus ($|E^*|$) master curve of the asphalt concrete layers using the FWD data. The estimated dynamic modulus master curve can be considered as “Level 2” inputs with regard to AASHTO’s *Mechanistic–Empirical Pavement Design*

Guide (MEPDG) input hierarchy. The $|E^*|$ curves generated by UGA-PAVE resemble (but are not actually) Level 1 inputs. Obtaining true Level 1 inputs for a dynamic modulus master curve requires site-specific data tested at different temperatures; however, FWD testing can only feasibly be conducted at a single temperature in situ.

To counteract this, a general time– temperature shifting (TTS) model for HMA is developed using results from GDOT RP 16-19 ⁽⁷³⁾, yielding:

$$\beta(T) = \alpha_1 T^2 + \alpha_2 T + \alpha_3 \quad (20)$$

Where, T is the desired temperature to shift to, α_i is the i^{th} TTS model coefficient, and β is the time– temperature superposition factor used to construct the $|E^*|$ master curve. The general TTS coefficients determined from RP 16-19 are $\alpha_1 = 0.0012$, $\alpha_2 = -0.1773$, and $\alpha_3 = 3.2262$. Using the above model, the time–temperature superposition shifting is performed according to:

$$\log_{10} f_R = \log_{10} f - \log_{10} \beta(T) \quad (21)$$

Where, f is the frequency of the pre-shift $|E^*|$ curve, and f_R is its corresponding reduced frequency for the master curve. In summary, using the above procedure allows UGA-PAVE to estimate $|E^*|$ inputs (i.e., dynamic modulus master curve) from an incomplete set of data (i.e., FWD testing conducted at a single temperature) and Level 2 data (i.e., the HMA time–temperature superposition model derived from RP 16-19).

METHOD

Limited FWD data are available; thus, only the GPR results for I-75N will be validated for subgrade modulus back calculation. The validation procedure is as follows. First, the densities, thicknesses, and estimated subgrade modulus along the road are calculated from the GPR data. Then, UGA-PAVE is

used to calculate the subgrade modulus at each FWD road station along I-75N using the layer densities and thicknesses measured by GPR. Finally, the subgrade moduli back calculated by the GPR and FWD methods are compared for validation.

FWD was conducted at 53 road stations along I-75N. The collection locations spanned 1 mile in total, beginning at milepost (MP) 239 and ending at MP 240, and the stations were spaced approximately 100 ft from each other. Six FWD drops were performed at each station: two 6-kip, two 9-kip, and two 12-kip drops. UGA-PAVE can produce one subgrade modulus prediction per FWD drop; thus, six modulus estimations were generated for each road station. The mean value of the six subgrade moduli was used as the FWD back calculated modulus at each road station.

RESULTS AND DISCUSSION

Before the GPR and FWD results were compared, a moving average was applied to the GPR data for clearer visualization of its trends. The moving average obtained for the validation was compared with the raw data set in figure 24. The averaged data were generated with a moving window size of 20 data points. More specifically, each point in the moving average was computed from the average of the current data point in the raw data and the 19 points to its left, or:

$$\bar{\rho}_i = \frac{1}{20} \sum_{j=0}^{19} \rho_{i-j} \quad (22)$$

Where, $\bar{\rho}_i$ is the i th point in the moving average, and ρ_{i-j} is the $(i - j)$ th point in the raw data. Note that for the first 19 data points (i.e., $1 \leq i \leq 19$), the window size (and therefore the denominator of the leading fraction) was less than 20 because no data points were available for $i < 1$.

The moving-averaged subgrade density extrapolated from the GPR data and the subgrade soil modulus back calculated from the FWD data via UGA-PAVE are compared in figure 25. The two data series were scaled independently to help identify persistent trends between the density and modulus values, and, in general, both series demonstrate convincing similarity between the two material properties. Note the GPR density data have been shifted to the left by 0.115 miles to obtain closer resemblance to account for possible errors in the locations recorded by GPR and FWD. The majority of the FWD back calculated moduli data consistently correspond to relatively similar values of density; in other words, the modulus data (red squares) often lie on or near to the moving-averaged subgrade densities (black line). This is most apparent for the data in the regions spanning 239.1 to 239.4 miles, 239.5 to 239.65 miles, and 239.8 to 239.9 miles.

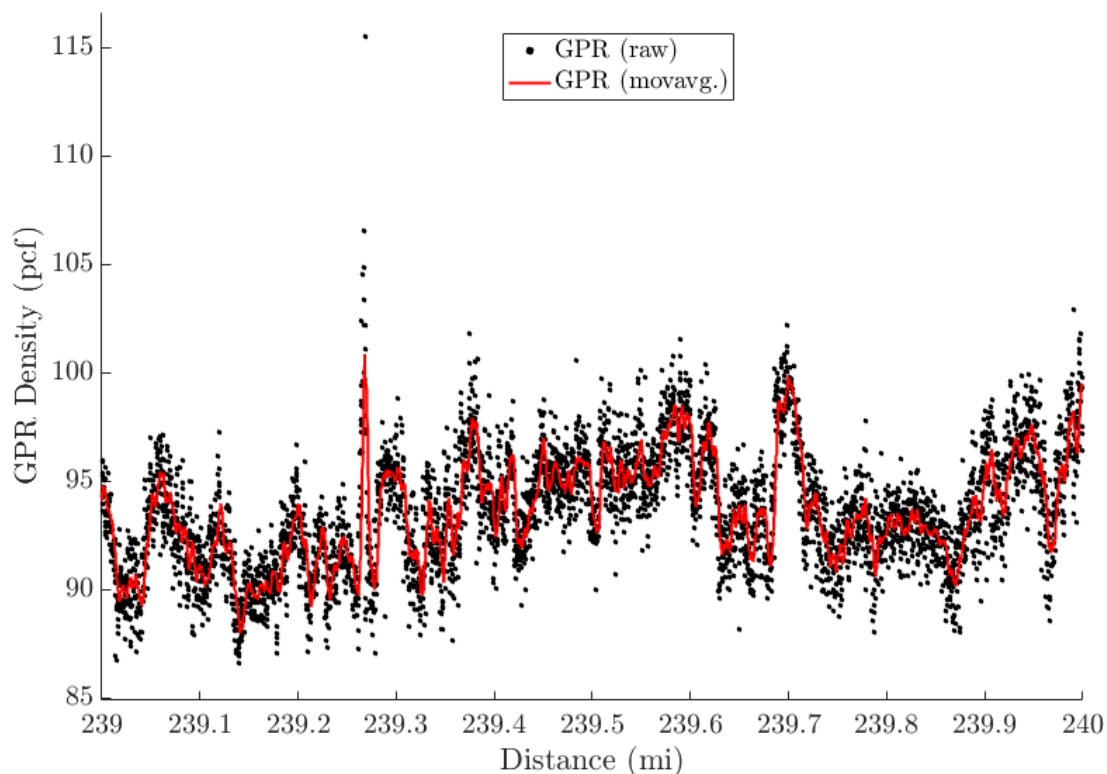


Figure 24. Graph. Comparison graph between the subgrade soil densities calculated from the raw GPR data (black) and its moving average (red).

There are a few notable regions of disagreement between the two series, namely the first three FWD

data points ranging from 239 to 239.05 miles, the four data points forming the trough around the 239.45 miles location, and the six data points around 239.7 miles. A characteristic common to the disagreeable data around 239.05 and 239.7 miles is that the modulus values are near 20 ksi, which was the maximum allowable modulus UGA-PAVE was able to consider for the subgrade during the back calculation. Such cases of the predicted modulus value being close to the high bound (i.e., at or near 20 ksi) often coincide with abnormal characteristics of the other pavement layers, which lead to inaccuracies in the back calculation. For example, in the case of an unusually weak asphalt concrete layer with an actual modulus below the minimum stiffness.

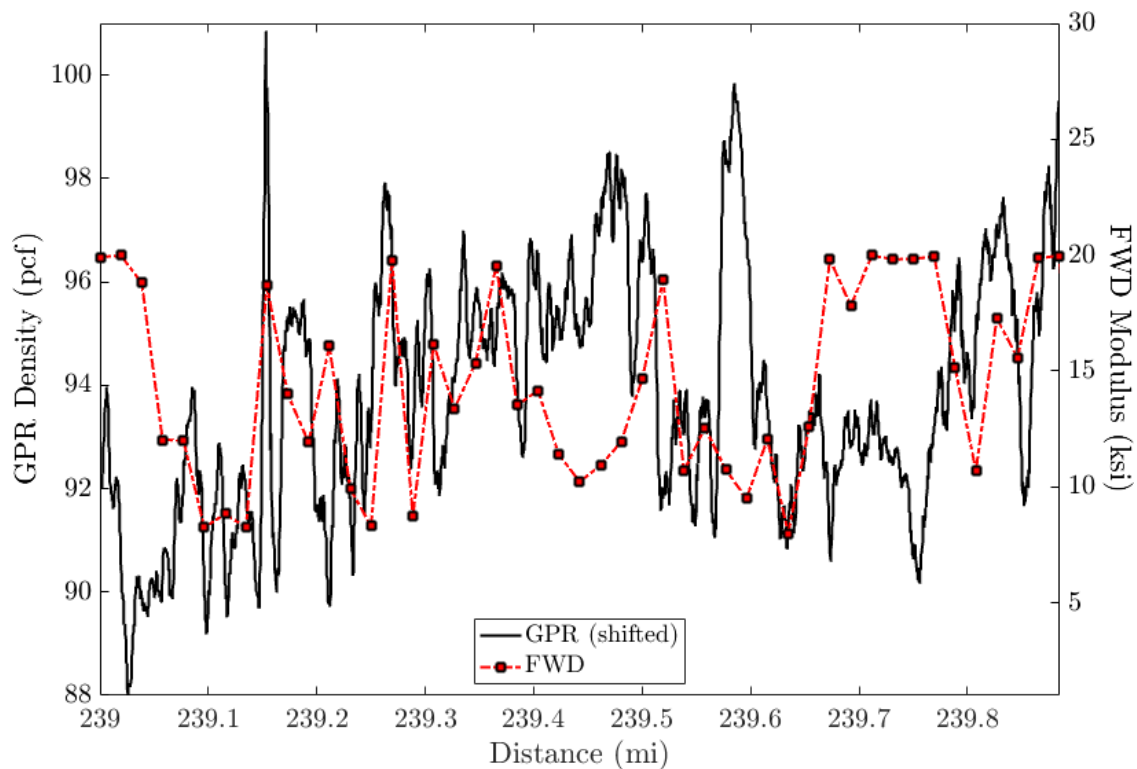


Figure 25. Graph. Comparison graph between the moving-averaged subgrade density calculated from GPR data (black) and the FWD-back calculated subgrade modulus from UGA-PAVE (red).

UGA-PAVE is allowed to consider, it tends to increase the predicted stiffness of the other layers (i.e., unbound aggregate base or subgrade layer moduli) to balance the predicted strength of the pavement

section as a whole. Thus, when overlooking the points corresponding to back calculated moduli near 20 ksi, the relative trends of the FWD back calculated moduli and GPR-derived densities agree well.

Conversely, the disagreeable values around 239.45 miles are notably lower than their corresponding GPR-predicted densities. The cause for this type of disagreement is harder to determine compared to the previously mentioned discrepancies. Possible reasons include a difference between the geometry (i.e., layer thicknesses) used in the pavement model compared to the in-situ pavement, or there may be other variables that affect the subgrade modulus–density relationship that were not accounted for in this preliminary study. Regardless, the satisfactory agreement overall between the GPR and FWD results suggests there can be great benefit from using the two methodologies in tandem.

SUMMARY

In this chapter, the subgrade densities calculated from GPR data and FWD back calculated subgrade modulus were compared for a mile stretch along I-75 beginning at MP 239. Analysis of the results suggest GPR can identify general trends in the variation of subgrade modulus. However, the study presented in this chapter is preliminary in nature, and a deeper investigation into the relationship between GPR-derived subgrade density and FWD back calculated subgrade modulus is recommended to obtain greater confidence in the relationship between the two back calculated material properties.

CHAPTER 6. NETWORK-LEVEL FIELD GPR DATA ACQUISITION AND ANALYSIS

In this chapter, the GPR subgrade density model is to be tested for its functionality in the network- level working roads. The data collection was made at a highway speed during the day without any traffic control, and during rush hours to test the quality and efficiency of using the UGA GPR van under difficult circumstances.

For scan purposes, the UGA GPR van with a dashboard mounted camera was employed to capture surface pavement conditions. Site surveys for the scanned critical state routes in GDOT District 7 were taken to obtain pavement profiles and surface distress imageries. Detailed information for the locations of tested road sections is summarized in table 14.

Table 14. Start/End coordinates of tested sections.

Route	Start/End	End/Start
I-20	33.654350531757494, -84.00724023768728	33.72411872624077, -84.8956737101354
I-85	33.91216454192528, -84.20822002414316	33.520149585408475, -84.62497202325831
I-75	34.079147675762556, -84.6531080313117	33.54689809812214, -84.27896706948752
I-285 ("the perimeter")	33.90184278444263, -84.27201914200613	33.89180578088741, -84.25901040949113

A total distance of 570 miles of critical state routes (slow lanes only of both driving directions) in District 7 was scanned with the UGA GPR van figure 26. The subgrade densities for four road sections (I-20, I-75, I-85, and I-285) were also estimated and the estimated subgrade density is represented through the online platform Kepler ⁽⁷⁴⁾ (<https://www.acqinfo.com/gpr/gpr/>).

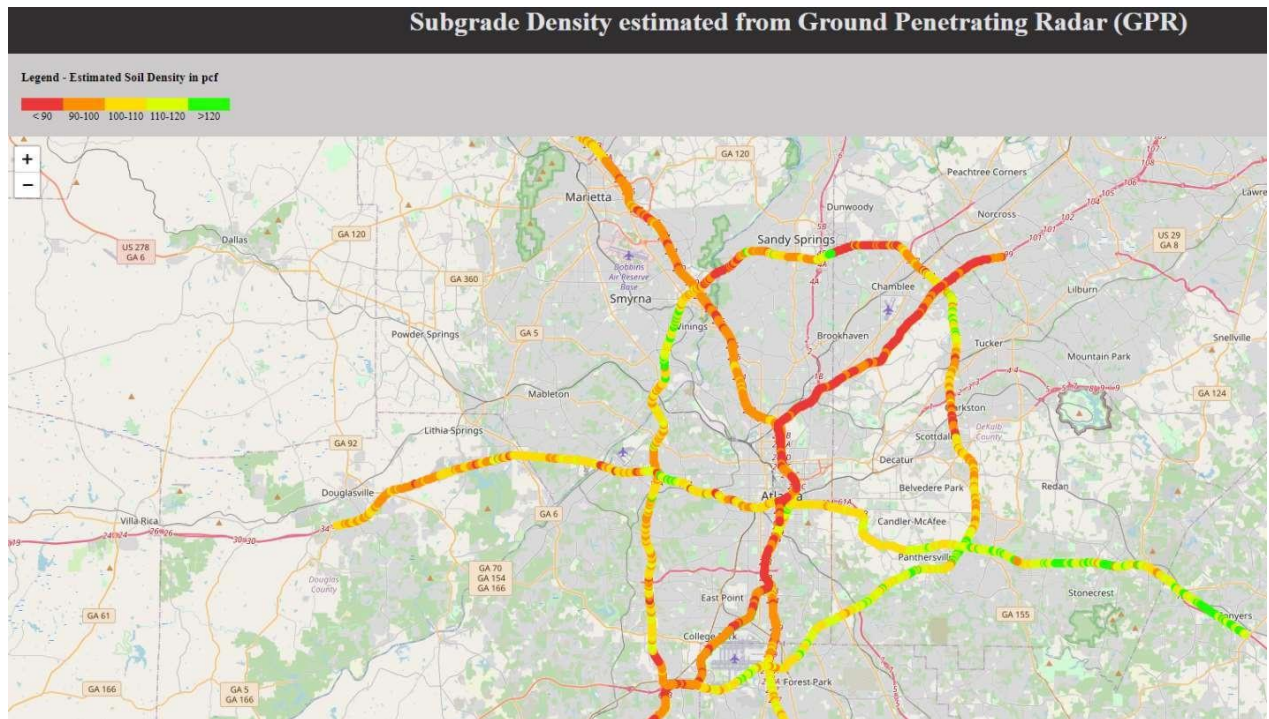


Figure 26. Map. scanned critical state routes in District 7.

Critical state routes inside District 7 are the following:

- I-20 East–West directions for 47 miles.
- I-285 connecting the three major interstate highways to Atlanta: I-20, I-75, and I-85; colloquially referred to as ‘the perimeter’.
- I-75 and I-85 extending in North–South directions for total distances of 160 miles.

The following section presents the analysis for these sections and discusses the differences between the density model implementation results for each section.

I-20 GPR SCAN RESULTS

47 miles of I-20 in the southbound slow lane were scanned with GPR. The results are summarized in table 15 and the suspected low-density sections for I-20 are presented in figure 27.

Table 15. I-20 (eastbound – slow lane) sections summary.

Route	Milepost		Average Density Value (pcf)	Average Water Content (%)
	from	to		
I-20 EB	34	49	95.45	19.4%
	50	53	103.52	24.4%
	54	59	98.73	20.3%
	60	82	108.01	26.3%

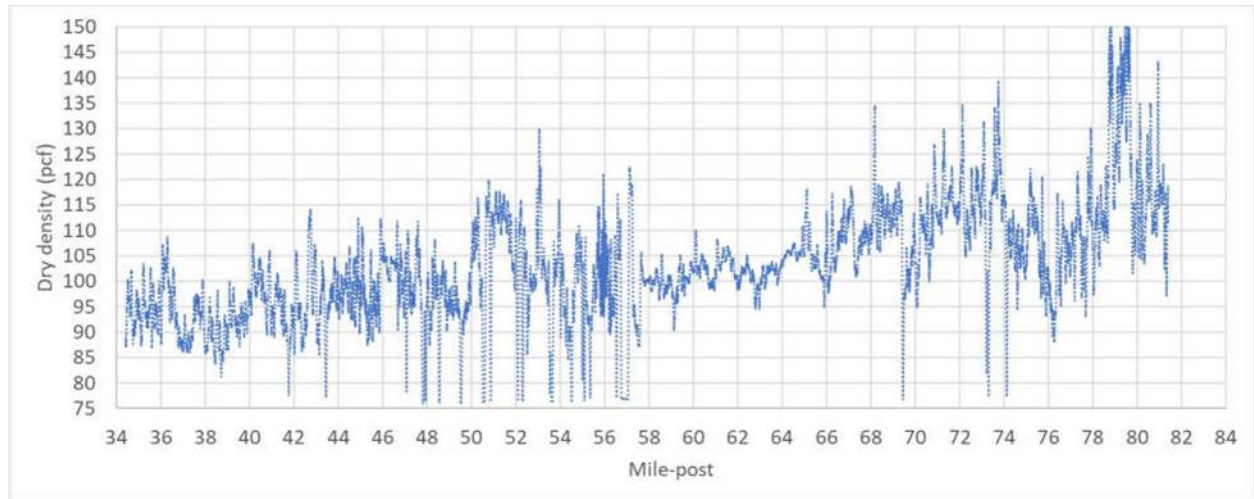


Figure 27. Graph. Estimated Subgrade soil density for I-20 (EB – slow lane).

For the I-20 scan section, weak spots where the subgrade soil density is relatively less than other sections are noticed in figure 27 and figure 28. Relatively weaker spot is visible between milepost 34 and milepost 49 with an average value for density of 95 pcf.

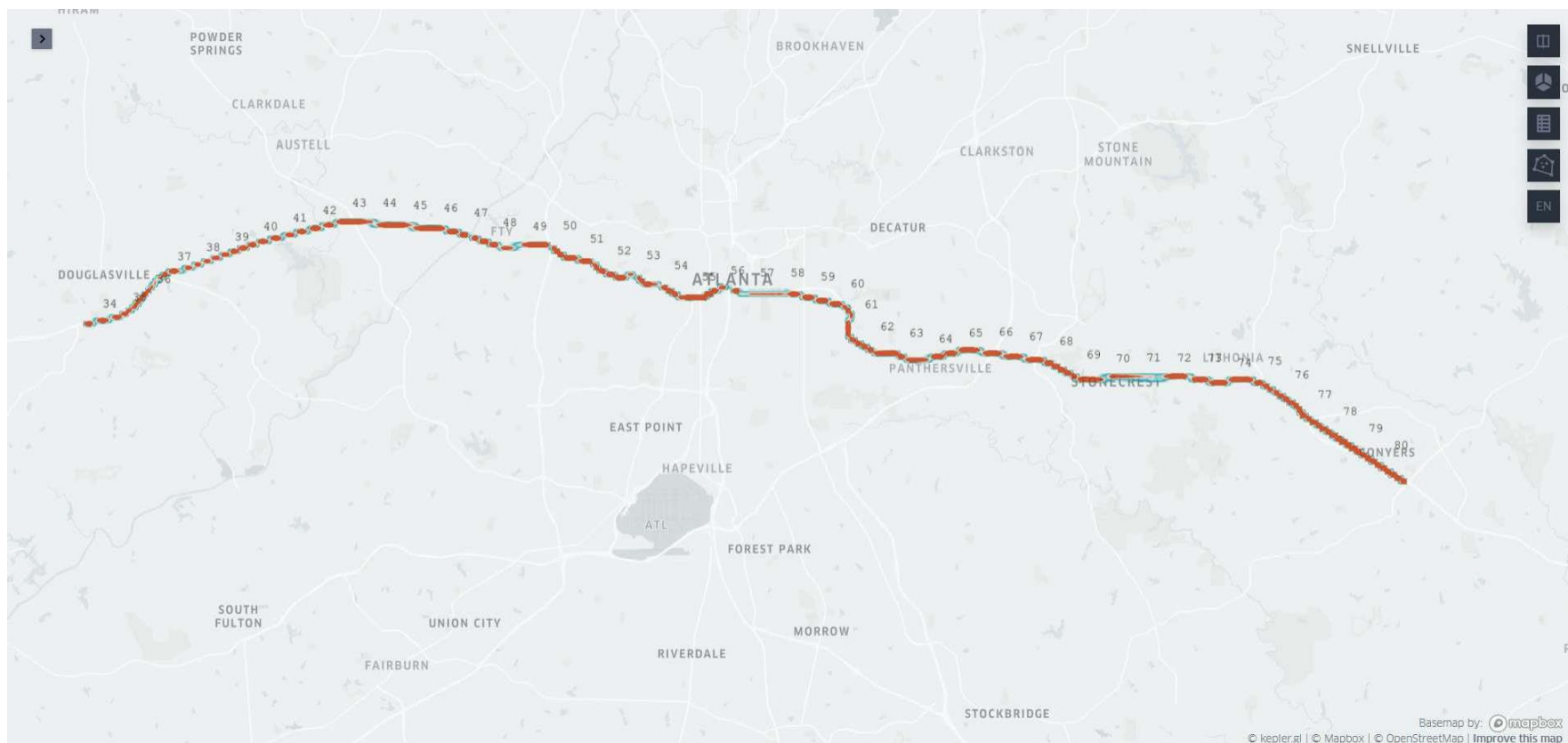


Figure 28. Map. I-20 scan (EB - slow lane)

I-75 GPR SCAN RESULTS

Forty miles on I-75 in the southbound direction and 48 miles in the northbound direction were scanned. The GPR scan results were used to calculate the dielectric constant of the subgrade soil, which was then used for calculating the soil dry density. Table 16 summarizes the dry density and water content change for different segments of I-75 northbound slow lane scan results. The results can be checked along the distance in figure 29 to figure 30, showing the variation in density of the subgrade soil along the road's stretch.

Table 16. I-75 (northbound – slow lane) sections summary.

Route	Milepost		Average Density Value (pcf)	Average Water Content (%)
	from	to		
I-75 (NB)	237	238	97.35	8.0%
	238	242	93.63	7.1%
	242	246	96.51	7.8%
	246	250	94.02	7.1%
	250	252	96.09	7.7%
	252	265	93.77	7.1%
	265	276	97.11	8.0%

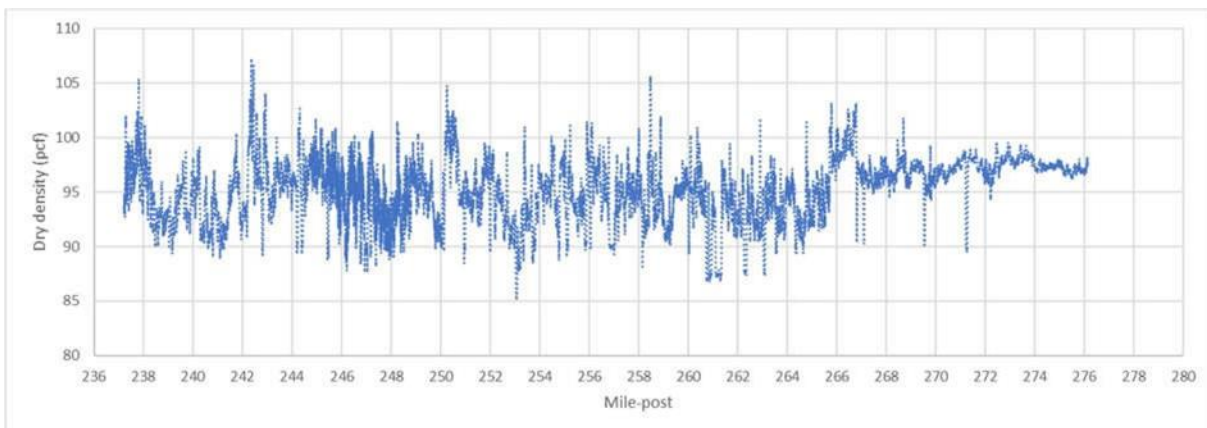


Figure 29. Graph. Subgrade soil density distribution for I-75 (NB – slow lane).

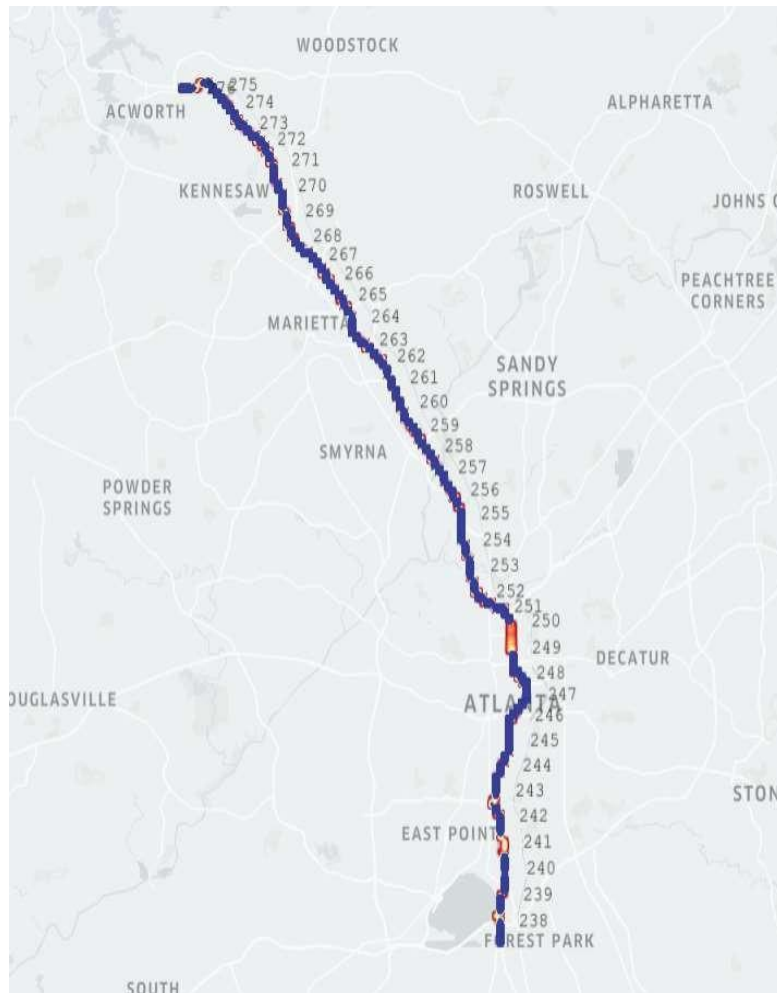


Figure 30. Map. I-75 scan (NB – slow lane)

The fluctuation of density values can be seen in different segments along the scanned section of I-75 northbound in the slow lane, with the weakest spot at milepost 238 to milepost 242 with an average value of 93 pdf dry density. Another weak spot with 93 pcf dry density extends from milepost 252 to milepost 265.

The variation between weak and strong segments of the scanned section of the I-75 southbound slow lane is shown in table 17, which summarizes the results of the scan process. The change in estimated subgrade density also can be visualized using figure 31 and figure 32.

Table 17. I-75 (southbound – slow lane) sections summary.

Route	Milepost		Average density value (pcf)	Average water content (%)
	from	to		
I-75 SB	277	264	104.41	10.0%
	264	254	94.75	7.7%
	254	252	99.31	7.8%
	252	248	92.90	7.3%
	248	242	97.62	8.4%
	242	240	93.18	7.3%
	240	236	105.98	10.1%
	236	233	94.48	7.8%
	233	229	99.92	9.2%

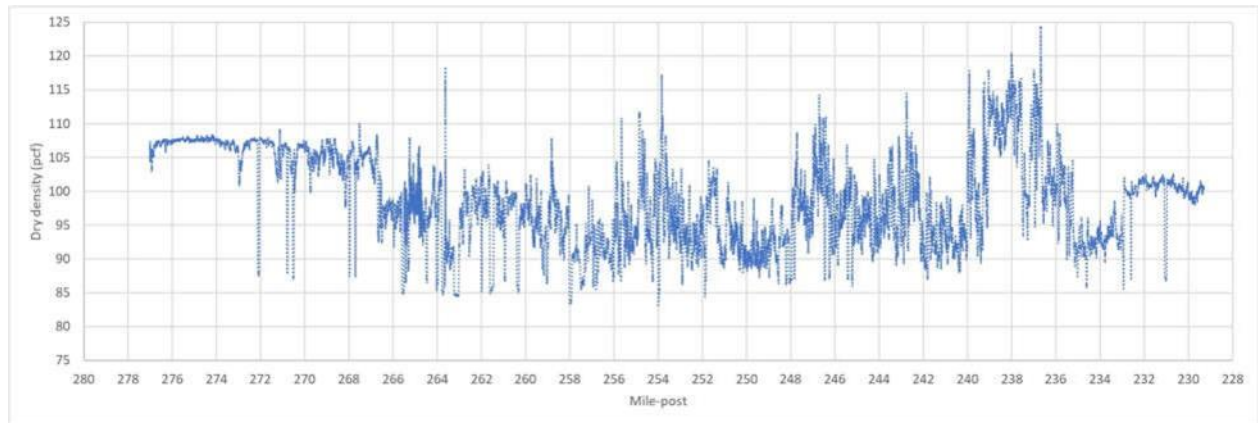


Figure 31. Graph. subgrade soil density distribution for I-75 (SB – slow lane).

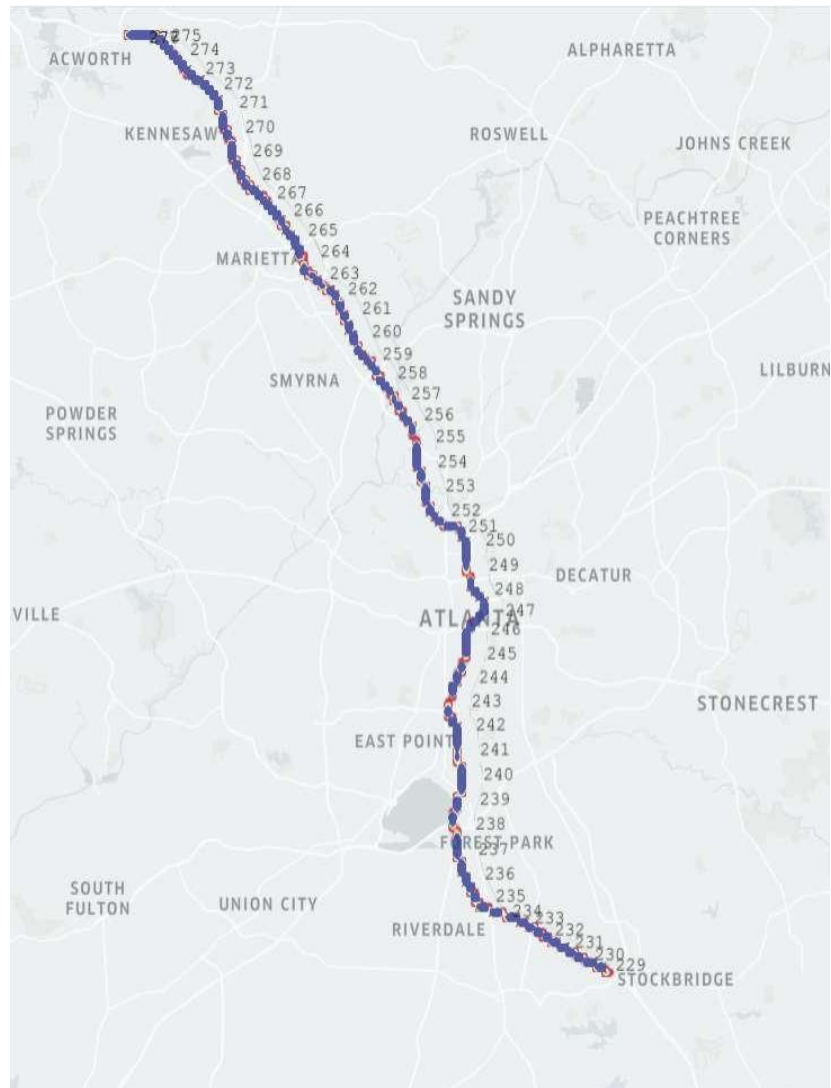


Figure 32. Map. I-75 scan (SB – slow lane).

I-85 GPR SCAN RESULTS

On I-85, 35 miles in the northbound slow lane and 40 miles in the southbound slow lane were scanned. table 18, figure 33, and figure 34 show the summary of the estimated subgrade dry density. For the I-85 southbound, the estimated subgrade dry density is consistent from milepost 61 to milepost 79. However, the variability of estimated subgrade density was observed from milepost 79 to milepost 99.

Table 18. I-85 (southbound – slow lane) sections summary.

Route	Milepost		Average Density Value (pcf)	Average Water Content (%)
	from	to		
I-85 SB	99	77	89.28	12.1%
	77	72	90.39	13.2%
	72	68	89.91	12.8%
	68	60	90.52	13.3%

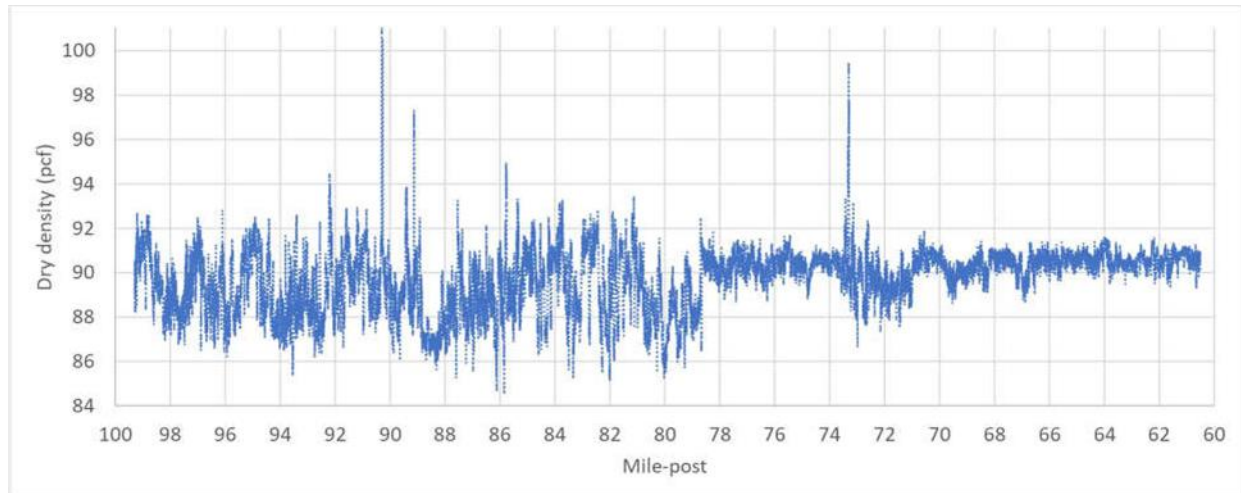


Figure 33. Graph. Subgrade soil density distribution for I-85 (SB – slow lane).

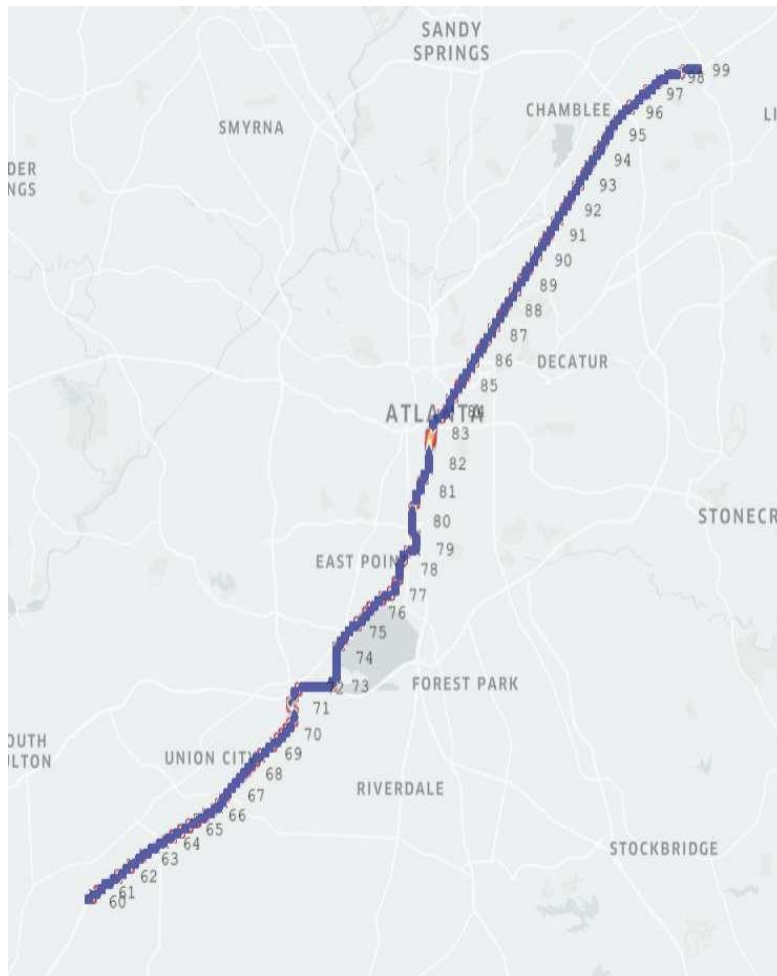


Figure 34. Map. I-85 sacn (SB – slow lane)

As shown in table 19, figure 35, and figure 36, the drastic change of the estimated subgrade density was observed. Overall, lower subgrade density was estimated in the segment of I-85 except for the section between milepost 71 to milepost 76.

Table 19. I-85 (northbound – slow lane) sections summary.

Route	Milepost		Average Density Value (pcf)	Average Water Content (%)
	from	to		
I-85 NB	63	69	98.75	14.1%
	69	70	90.32	11.9%
	70	77	107.71	46.4%
	77	97	90.49	11.9%

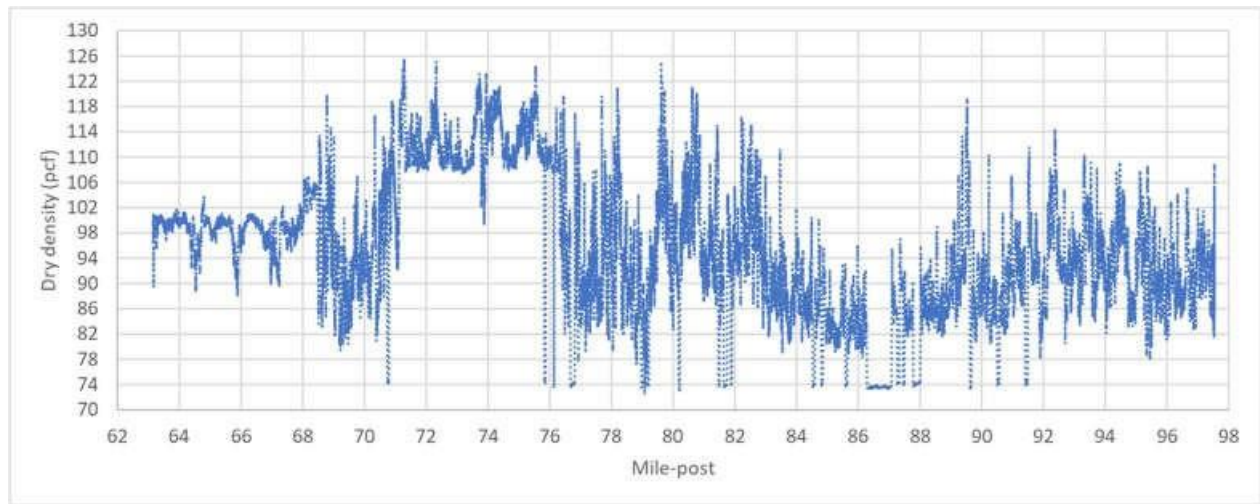


Figure 35. Graph. Subgrade soil density graph for I-85 (NB – slow lane).

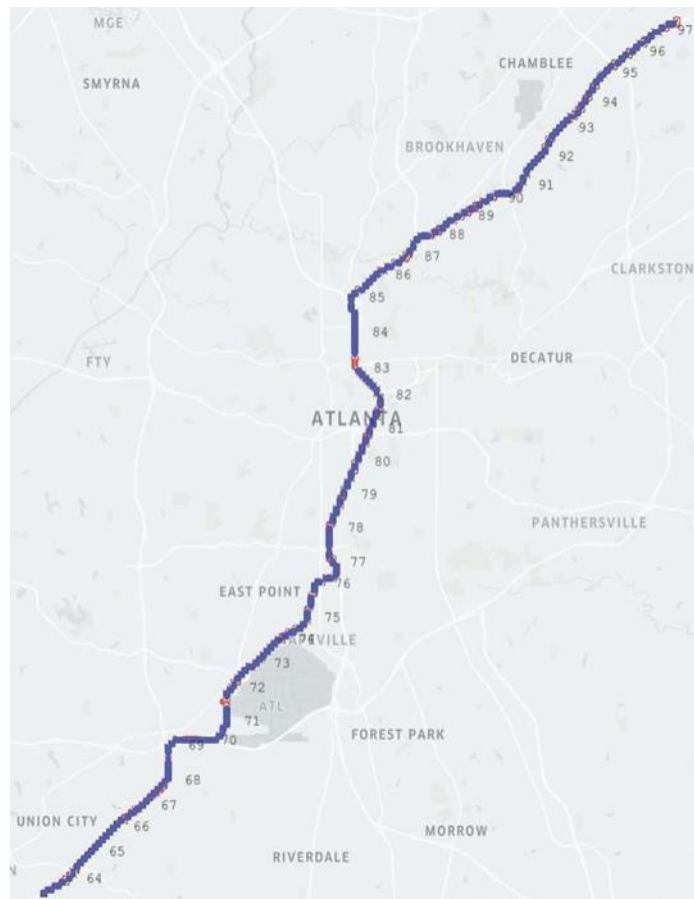


Figure 36. Map. I-85 scan (NB – slow lane)

I-285 GPR SCAN RESULTS

Fifty-eight miles for the inside circle and 61 miles for the outside circle (slow lane) were scanned on the I-285 loop. The scan results of the GPR frequency reflections were used to calculate the dielectric constant and density of the subgrade soil.

The calculation results are presented in table 20 and figure 37. Figure 38 represents the Kepler platform map for the density distribution of the subgrade soil.

The scanned section has two segments at mileposts 18–28 and 49–64 that require further attention and deeper investigation.

Table 20. I-285 (inner loop – slow lane) sections summary.

Route	Milepost		Average Density Value (pcf)	Average Water Content (%)
	from	to		
I-285 IB	28	36	88.84	5.5%
	36	49	92.77	6.8%
	49	53	88.48	5.3%
	53	57	92.22	6.4%
	57	62	88.20	5.2%
	62	20	93.33	7.0%
	20	25	89.27	5.3%
	25	28	94.85	6.9%

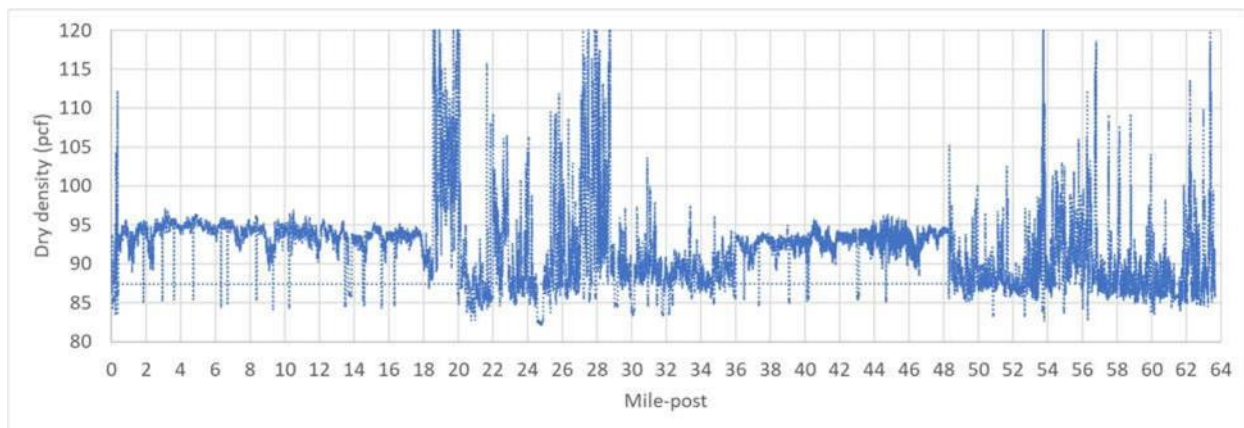


Figure 37. Graph. Subgrade soil density graph for I-285 (inner loop).

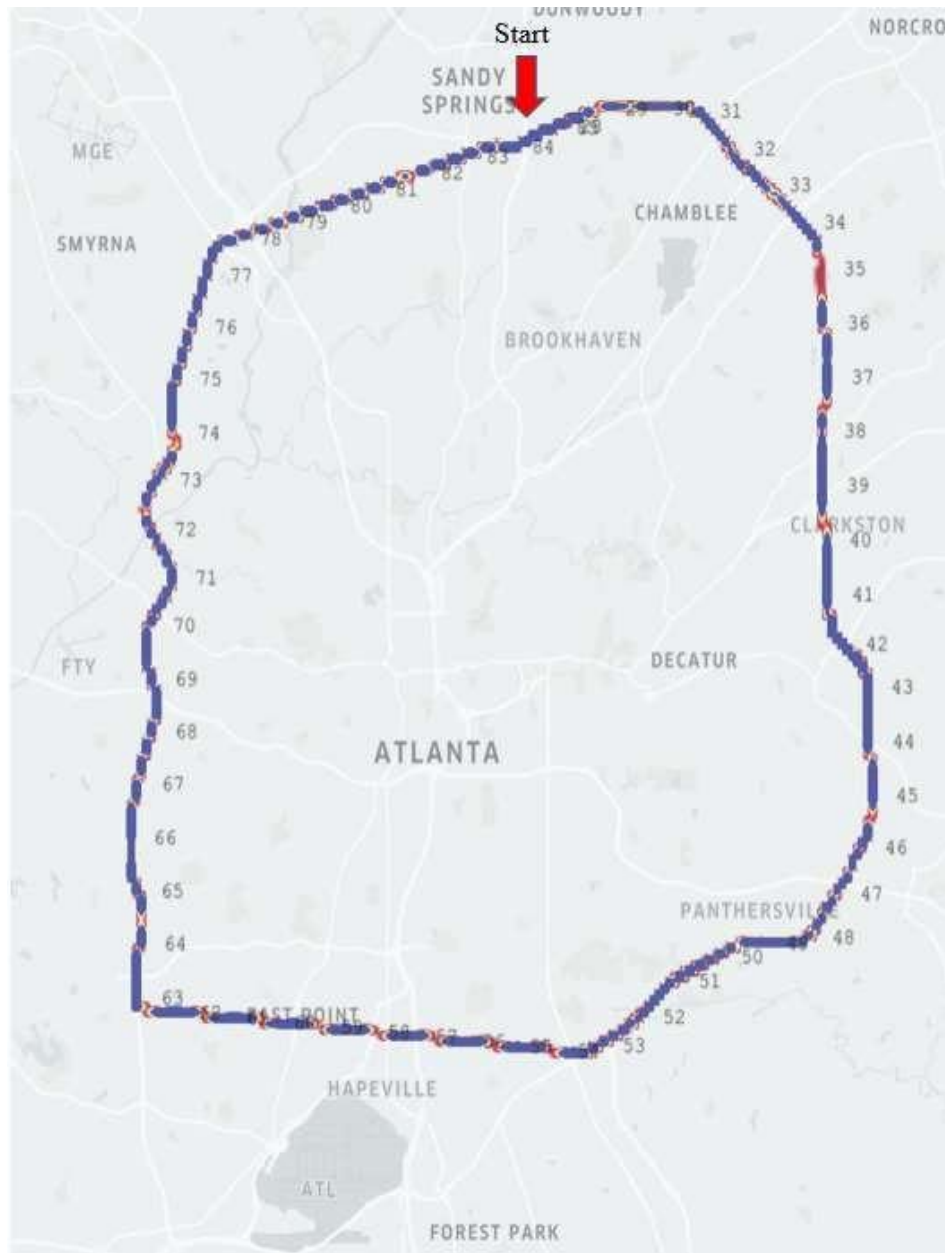


Figure 38. Map. I-285 scan (inner loop)

The density was more consistent for the outer loop than the inner loop with an average density value of 95–100 pcf. Weak sections are noticed below the threshold of 95 pcf as shown in table 21. Also, dry density variation along the scanned section is shown in figure 39 and figure 40.

Table 21. I-285 (outer loop – slow lane) sections summary.

Route	Milepost		Average Density Value (pcf)	Average Water Content (%)
	from	to		
I-285 OB	26	21	99.84	8.3%
	21	19	91.07	5.9%
	19	11	97.79	8.0%
	11	9	88.71	5.1%
	9	0	99.61	8.5%
	0	53	92.43	6.5%
	53	34	98.03	8.1%
	34	29	92.36	6.4%

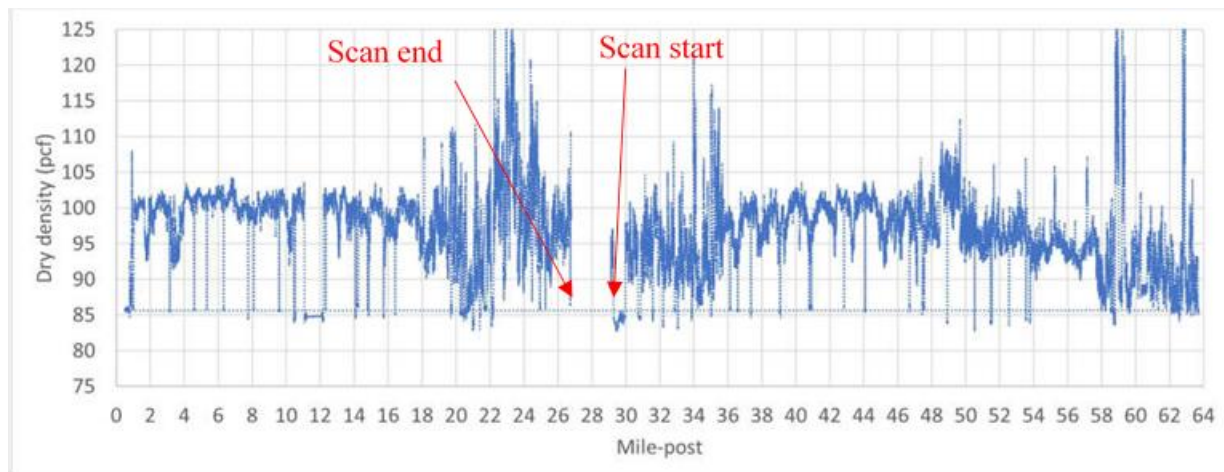


Figure 39. Graph. Subgrade soil density graph for I-285 (outer loop).

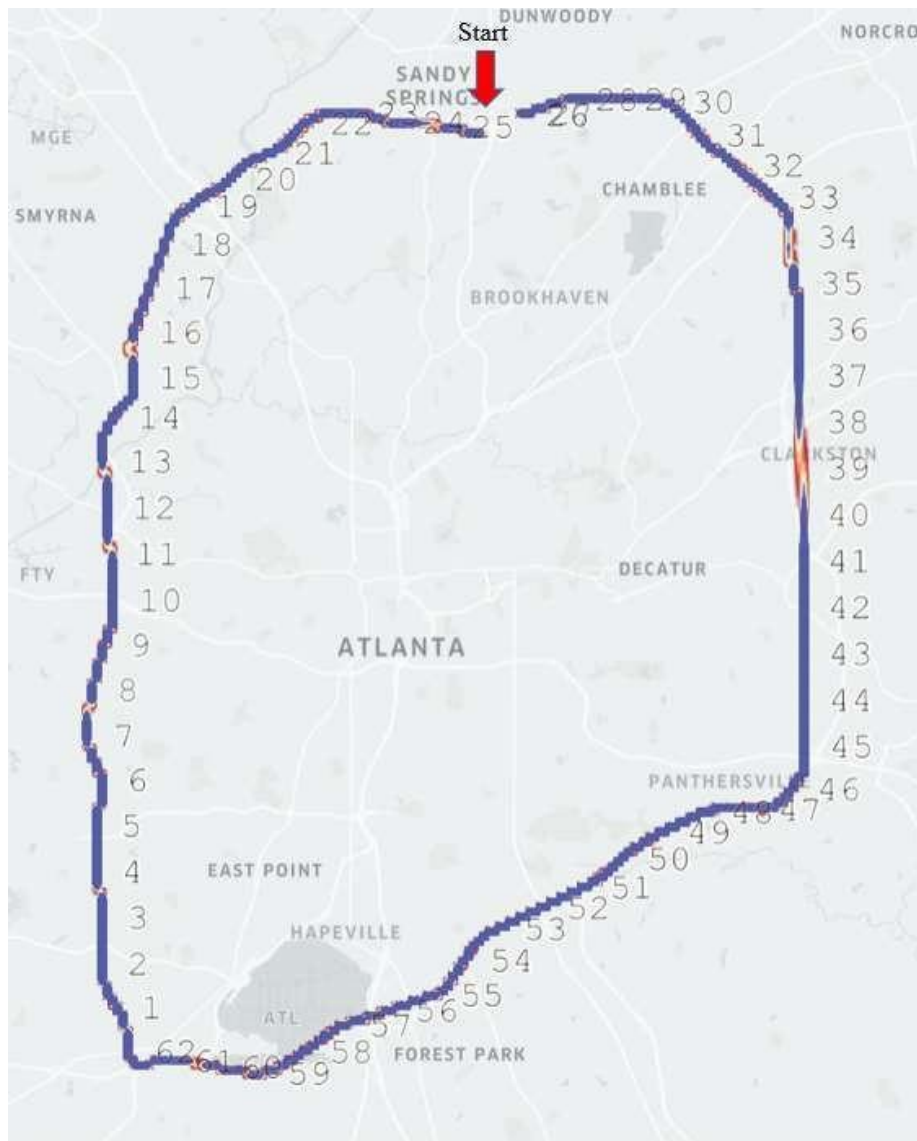


Figure 40. Map. I-285 scan(outer loop)

Figure 41 and table 22 summarize the critical sections with low subgrade density values along the scanned sections. These sections are considered potential weak subgrade sections that need attention for future maintenance and rehabilitation plan.

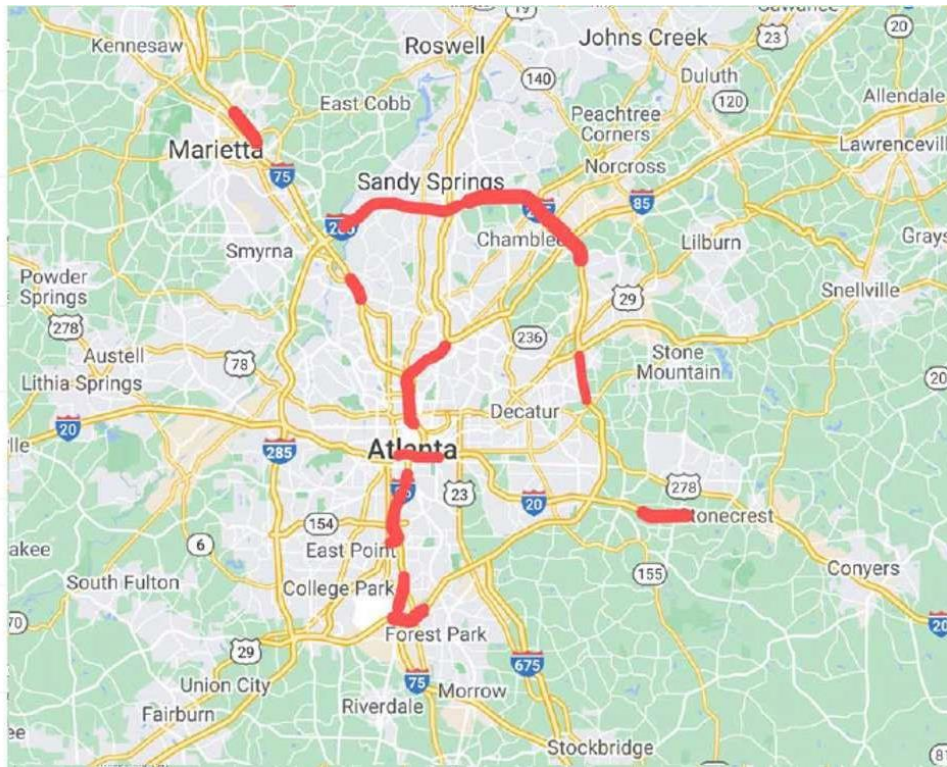

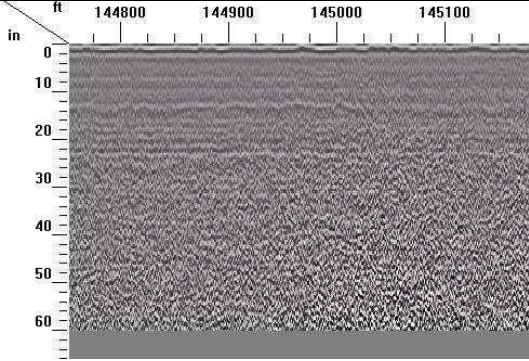

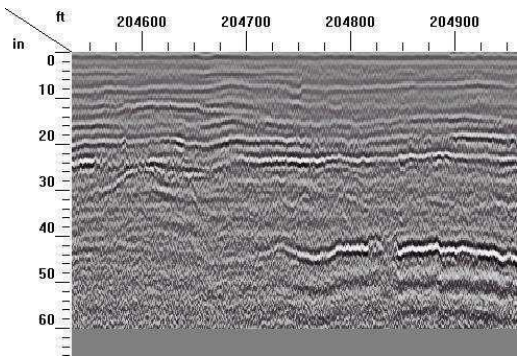

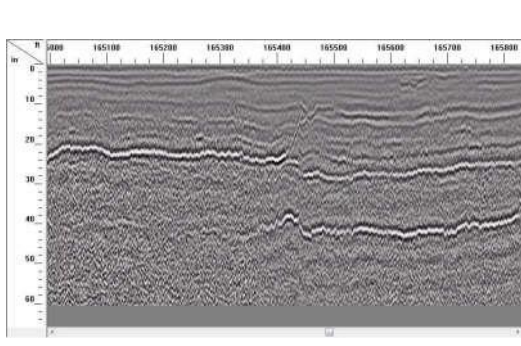

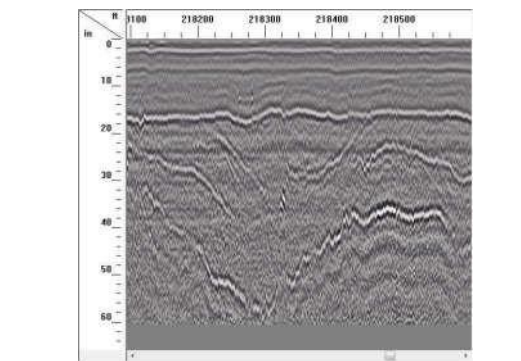


Figure 41. Map. weak spots for critical state routes in District 7 – Slow lane.


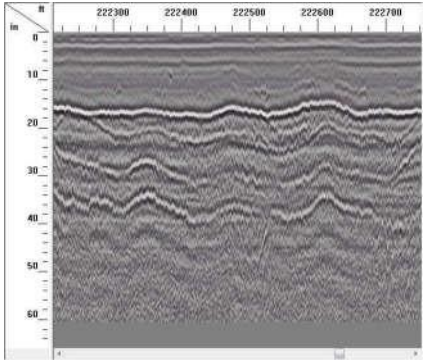

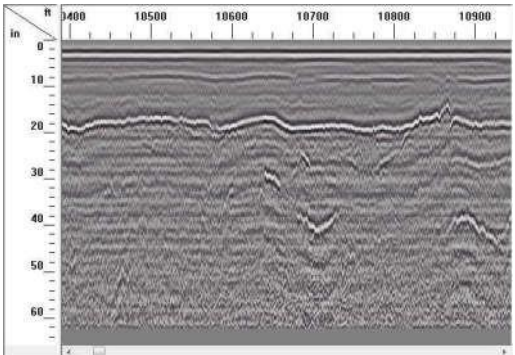
Table 22. Critical sections output example.

Route	Milepost		Average Density Value (pcf)	Average Water Content (%)	Surface Image (example)	GPR Image
	from	to				
I-20 EB	34	49	95.45	19.4%		
	54	59	98.73	20.3%		


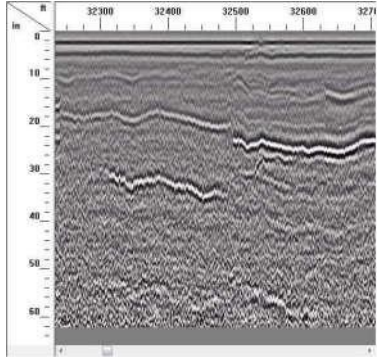

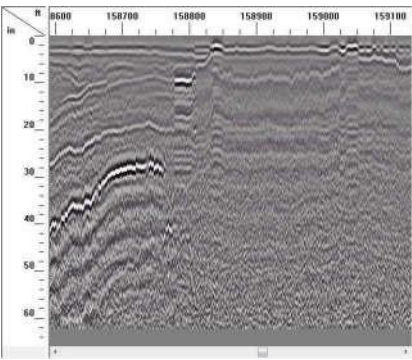
cont. Table 22. Critical sections output example.

Route	Milepost		Average Density Value (pcf)	Average Water Content (%)	Surface Image (example)	GPR Image
	from	to				
I-75 SB	264	254	94.75	7.7%		
	252	248	92.90	7.3%		


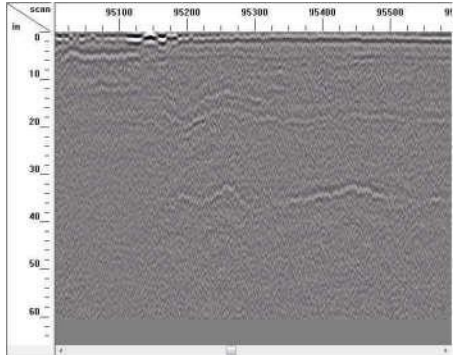

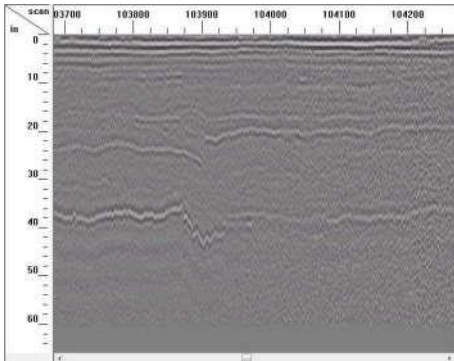
cont. Table 22. Critical sections output example.

Route	Milepost		Average Density Value (pcf)	Average Water Content (%)	Surface Image (example)	GPR Image
	from	to				
I-75 SB	242	240	93.18	7.3%		
I-75 NB	238	242	93.63	7.1%		


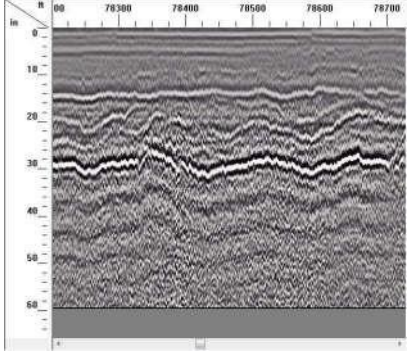

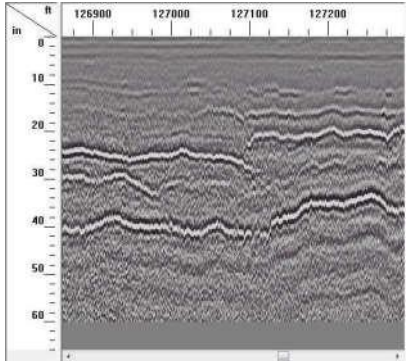
cont. Table 22. Critical sections output example.

Route	Milepost		Average Density Value (pcf)	Average Water Content (%)	Surface Image (example)	GPR Image
	from	to				
I-75 NB	246	250	94.02	7.1%		
	252	265	93.77	7.1%		

cont. Table 22. Critical sections output example.

Route	Milepost		Average Density Value (pcf)	Average Water Content (%)	Surface Image (example)	GPR Image
	from	to				
I-85 SB	99	77	89.28	12.1%		
	72	68	89.91	12.8%		

cont. Table 22. Critical sections output example.

Route	Milepost		Average Density Value (pcf)	Average Water Content (%)	Surface Image (example)	GPR Image
	from	to				
I-85 NB	69	70	90.32	11.9%		
	77	97	90.49	11.9%		

CHAPTER 7. CONCLUSIONS AND RECOMMENDATIONS

This study investigates the possibility of detecting changes of subgrade density and modulus by using GPR in the physical characteristics of road materials. In this study, an air-coupled pulsed radar system for collecting GPR signals was used in the time domain, whose frequency spectra were then analyzed for variations in density values.

CONCLUSIONS

The main research objective was to develop and validate the potential of a self-consistent method based on the analysis of the GPR signal in the frequency domain to describe the spatial variability of subsurface moisture and subgrade dry density. This method is of interest to a large variety of nondestructive applications. Based on the results of this study, the following conclusions are drawn:

- Subsurface moisture content can be inferred by permittivity measurements through GPR.
- The proposed semi-empirical relationship for subgrade dry density prediction is appropriate for the investigated fine-grained soil types. For higher water content values, the relationship mainly overestimates the expected dry density, independently from soil texture. In addition, the prediction is more accurate for low-moisture soils within the entire range of soils surveyed.
- The relative dielectric permittivity increases as a function of density value. In other words, the greater the material's compaction, the higher its relative permittivity.
- The proposed model predicts subgrade soils dry density with an overall error less than 11 percent in most of the surveyed stations.

RECOMMENDATIONS

Specific recommendations are given below:

- Exercise caution when averaging GPR traces to be used as a reference signal for representing deformation properties of the investigated medium. It is highly recommended to have full knowledge of the influence domain of the instrument providing for the ground-truth measurement of dry density.
- Focus future research on different ranges of frequencies and estimation of soil's mechanical (i.e., strength and elasticity) properties from GPR data.
- Although the GPR system has proven its capability and potential to be a quick tool for evaluation of the structural integrity of the service roads, it still needs field validation for network-level roads.
- It is believed that the studies comparing GPR and FWD data can be greatly beneficial to GDOT. Analysis of the preliminary results from I-75N suggest GPR is capable of identifying general trends in variation of subgrade density and modulus. However, a deeper investigation into the relationship between GPR-derived subgrade density and FWD back calculated subgrade modulus is recommended. The expected benefit of determining an accurate relationship between the two methodologies is that GPR can be used as an initial “wide-tooth comb”, which can quickly identify locations of atypical/abnormal/unexpected pavement characteristics. Then, FWD testing can be conducted at those locations and serve as a “fine-tooth comb”, which takes more time to conduct/process but has higher accuracy.

APPENDIX A. PROPOSED GDT TEST METHOD

GDT test method for evaluating subgrade soil condition density/water content/surface using a ground-penetrating radar (GPR) system.

GDT #TBD

Rev. ###/##/21

GDT #TBD

A. Scope

Use of the GPR scan system developed by the UGA-Geomaterials lab to investigate the physical condition of subgrade soil (dry density and water content).

B. Apparatus

The apparatus consists of the following:

1. Ground-penetrating Radar (GPR) 2 GHz antenna
2. Ground-penetrating Radar (GPR) 400 MHz antenna.
3. GPS device compatible with GPR control unit
4. Operating control unit GSSI SIR-30.
5. GPR Manufacturer's Instruction Manual
6. Post-processing Software License and User's Guide
7. Front mounted dash camera
8. Pavement surface mounted dash camera

C. Sample Size and Preparation

No sample preparation is needed

D. Procedures

Field Data Collection

1. GPR data shall be collected when the pavement surface is NOT wet or moist. The data collection must be conducted within the recommended operating temperature in the Manufacturer's Instruction Manual.
2. To operate the GPR unit, follow the procedures shown in the Manufacturer's Instruction Manual accompanying the unit.
3. Mount the antennas to their seating position and the specified heights above the ground.
 - 2 GHz antenna – Air coupled antenna (19" above pavement surface)
 - 400 MHz antenna – Ground coupled antenna (4" max. above pavement surface)
4. Connect the GPR unit to the SIR 30 control unit.
5. Mount the GPS unit into the proper position close to the antennas and connect it to the GPR control unit. Make sure it reads the actual coordinates before starting the scan.
6. Measure the distance between GPS antenna and centroids of Antennas for the data collection entries.
7. Select parameters and preload setups recommended in the Manufacturer's Instruction Manual accompanying the unit. If a manual entry is required, the following parameter settings are recommended as a starting point for calibration:
 - Dielectric constant: 5–8 (for Pavement)
 - Antenna frequency: 1–2 GHz
 - Transmit rate: 100 KHz
 - Sampling rate: 75 scans per second (to maintain 1 scan per foot at speed of 55 mph)
8. Attach and switch on the dash cameras to run, secure the connection of the two dash cameras to get synchronized footage of the front view and pavement surface, and assure that the dash cams are collecting coordinates that match these of GPR units.

9. Perform the calibration over the copper plate and save the collected reading using the current date for the data processing purposes.
10. Set up your file settings (name/location/any additional info), then start the scan.
11. After the end of the scan, save the scan and import it to a hard drive for data processing.

Data Post Processing

1. Post-processing software program compatible with the stored file format shall be used.
2. Basic post-processing steps that are recommended in the post-processing software user's guide should be applied to the collected dataset. This basic data processing should leave the original dataset intact such that it does not distort the information.
 - It should be recognized that excessive filtering could drastically alter the overall dataset.
3. Apply background removal filtering.
4. Detect the base line for data to rely on using ground function from analysis software (RADAN7).
5. Define the pavement surface level (1st layer interface).
6. Manually detect the layer interfaces using the procedures in the Manufacturer's Instruction Manual until reaching the desired layer for the whole scanned section.
7. Extract the interpolated values (frequency – amplitude values) over the layer interface to a spreadsheet for the data processing.
8. Extract the data from calibration file for the reflections over copper plate (A_m)

E. Calculations

For calculation of density, several calculation processes must be applied, including some initial assumptions.

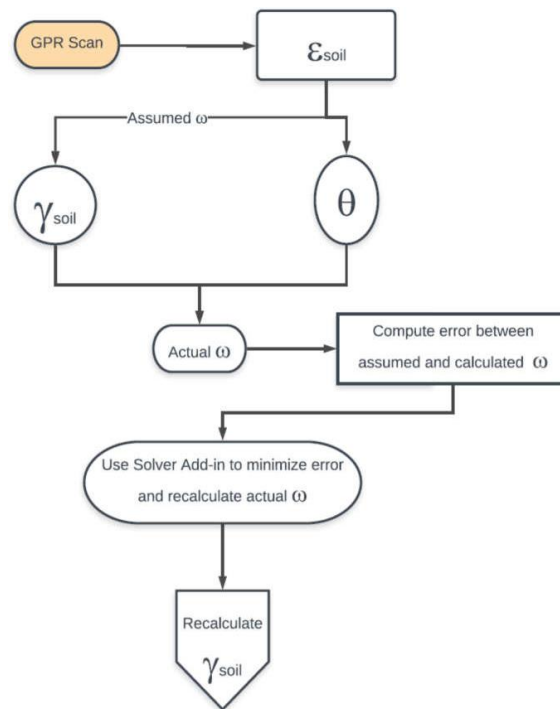


Figure 42. Chart. Density Model Implementation

9. Dielectric constant (ϵ) for targeted layers is calculated according to the following equations, depending on the location of the layer: first layer (equation 23), second layer (equation 24), or third layer (equation 25 and 26).

$$\varepsilon_1 = \left(\frac{1 + \frac{A_0}{A_m}}{1 - \frac{A_0}{A_m}} \right)^2 \quad (23)$$

$$\varepsilon_{\text{Base}} = \varepsilon_{\text{HMA}} \left(\frac{1 - \left(\frac{A_0}{A_m} \right)^2 + \left(\frac{A_{\text{Base}}}{A_m} \right)}{1 + \left(\frac{A_0}{A_m} \right)^2 - \left(\frac{A_{\text{Base}}}{A_m} \right)} \right)^2 \quad (24)$$

$$\varepsilon_{r,n} = \varepsilon_{r,n-1} \left(\frac{1 - \left(\frac{A_0}{A_m} \right)^2 + \sum_{i=1}^{n-2} \gamma_i \left(\frac{A_i}{A_m} \right) + \left(\frac{A_n}{A_m} \right)}{1 - \left(\frac{A_0}{A_m} \right)^2 + \sum_{i=1}^{n-2} \gamma_i \left(\frac{A_i}{A_m} \right) - \left(\frac{A_n}{A_m} \right)} \right)^2 \quad n > 2 \quad (25)$$

$$\gamma_i = \frac{\sqrt{\varepsilon_{r,i}} - \sqrt{\varepsilon_{r,i+1}}}{\sqrt{\varepsilon_{r,i}} + \sqrt{\varepsilon_{r,i+1}}} \quad (26)$$

10. Assume a water content value (as a starting point) for the density equation.
11. Calculate initial density value using equation 27.

$$\therefore \gamma_d = \frac{(\sqrt{\varepsilon_{\text{soil}}} - 1)}{\frac{1}{G S} (\sqrt{\varepsilon_s} - 1) + w (\sqrt{\varepsilon_w} - 1)} \quad (27)$$

12. Calculate the volumetric water content (θ) using the Topp equation (29) and the calculated dielectric constant from step 1.

$$\theta = -0.053 + 0.0292 (\varepsilon_{\text{soil}}) - 5.5 \times 10^{-4} (\varepsilon_{\text{soil}})^2 + 4.3 \times 10^{-6} (\varepsilon_{\text{soil}})^3, \quad (28)$$

13. Recalculate soil bulk density using assumed water content and the calculated dry density.
14. Use both volumetric water content and initial bulk density to recalculate water content.
15. Calculate the error between the assumed water content from step 2 and the calculated water content from step

$$[\text{Error} = ((\text{Calculated} - \text{Assumed}) / \text{Calculated})^2] \quad (29)$$

16. Minimize the error and recalculate the correct values. This can be done using the Solver in Microsoft Excel.
17. Use the newly calculated water content value from step 8 to recalculate the soil dry density
18. Apply equation 31 using database values for a and b to recalculate the dry density.

$$\gamma_{\text{dry, estimated}} = \alpha (\gamma_{\text{dry, calculated}})^\beta \quad (30)$$

19. If ground-truth values for the targeted layer's dry density are available, apply the same procedure of error minimizing technique from step 7 between actual values and estimated values for dry density from step 9 using base equation 31 and recalculate a and b for further research or application.

20. Examples of Calculations:

For illustration purposes, an example for calculating the dry density using lab data is shown below. Given:

$A_m = 7,942,173$ (frequency over metal plate), $\varepsilon_w = 80$ (dielectric water constant for water)

$\varepsilon_s = 15$ (Working from experience, we must know the soil type to add this value. The value here is the dielectric constant for silty soil.)

$A_o = 5,450,763$ (collected frequency value over the tested sample)

- a. Calculate tested sample dielectric constant, $\varepsilon_{\text{soil}} = 28.90$.
- b. Assume water content value $w_{\text{ass}} = 10\%$.
- c. Calculate initial density value, $\gamma_{\text{dry init.}} = 2.348 \text{ t/m}^3$.

- d. Volumetric water content, $\theta = 44\%$.
- e. Recalculate bulk density value, $\gamma_{\text{dry bulk}} = 1.996 \text{ t/m}^3$.
- f. Recalculate water content, $w_{\text{recal}}\% = 17\%$.
- g. Error = 40%.
- h. Using the Solver equation to minimize error finds the calculated $w\% = 23\%$ (actual measured $w\% = 19\%$ with error value of 21%).
- i. Recalculate initial density value, $\gamma_{\text{dry est}} = 1.511 \text{ t/m}^3$.
- j. $\alpha = 1.464$, $\beta = 0.171$ from this research database, $\gamma_{\text{dry recalculated}} = 1.571 \text{ t/m}^3$ (actual measured $\gamma_{\text{dry}} = 1.673 \text{ t/m}^3$ with error value of 6%).

F. Calibration Procedure

The survey (or travel) distance depth/pavement layer thickness must be calibrated in accordance with the Manufacturer's Instruction Manual.

The calibration process involves collecting a reading over a copper plate to ensure the thicknesses and height of antenna are appropriate for starting the road scan.

Note: The success of GPR calibration/operation depends on the operator's knowledge of which GPR device he/she is operating and background knowledge of the technology.

G. Report

1. The GPR inspector shall report the results and locations of spots with density below a pre-decided density threshold.
2. Extract dash cam images for the same locations with low density for deeper and further analysis.

ACKNOWLEDGMENTS

The University of Georgia acknowledges the financial support for this work provided by the Georgia Department of Transportation (GDOT). The authors thank technical manager, Mr. Ian Rish, and his Office of Materials and the project manager, Mr. Brennan Roney, who advised the research team in successfully performing the study and assisted in the coordination of project meetings with GDOT. Finally, the team expresses thanks for the continuous support from Mrs. Supriya Kamatkar and her leadership in the Performance-based Management and Research Office.

REFERENCES

1. Romero, P. and Kuhnaw, F. (2002). “*Evaluation of New Non-nuclear Pavement Density Gauges with Data from Field Projects.*” Transportation Research Record: Journal of the Transportation Research Board, 1813, Transportation Research Board of the National Academies, Washington, DC, pp. 47–54.
2. Lay, M. G. (1992), “*Ways of the World : A History of the World’s Roads and of the Vehicles That Used Them.*” Rutgers University Press.
3. O’Flaherty, C., Butterworth-Heinemann.Pellinen, T., Witczak, M., and Bonaquist, R. (2002). “*Asphalt Mix Master Curve Construction Using Sigmoidal Fitting Function with Non-linear Least Squares Optimization.*” 15th ASCE Engineering Mechanics Division Conference, New York, June 4. Available online: [https://doi.org/10.1061/40709\(257\)6](https://doi.org/10.1061/40709(257)6).
4. Watson. (1994). “*Highway construction and maintenance*”, 2nd Ed., Longman, Essex, U.K.
5. Evans, R.D. (2010). “*Optimizing Ground Penetrating Radar (GPR) to Assess Pavements.*” EngD. thesis, Loughborough University, England. Available online: <https://hdl.handle.net/2134/20465>.
6. Kennedy, C.K. and Lister, N.W. (1978). “*Prediction of Pavement Performance and the Design of Overlays.*” Report LR 833, Transport and Road Research Laboratory (TRRL), Crowthorne, UK.
7. Maierhofer, C. (2010). “*Planning a Non-destructive Test Programme for Reinforced Concrete Structures*”. Woodhead Publishing Limited. Vol. 2. Chapter 1. pp. 3–13.
8. Beutel, R., Reinhardt, H.W., Grosse, C.U., Glaubitt, A., Krause, M., Maierhofer, C., Algernon, D., Wiggenshauser, H., and Schickert, M. (2008). “*Comparative Performance Tests and Validation of NDT Methods for Concrete Testing.*” Journal of Nondestructive Evaluation, 27, pp. 59–65.
9. Dérobert, X., Iaquina, J., Klysz, G., and Balayssac, J.P. (2008). “*Use of Capacitive and GPR Techniques for the Non-destructive Evaluation of Cover Concrete.*” NDT&E International, 41, pp. 44–52.
10. Dérobert, X. and Berenger, B. (2010). “*Non-destructive Evaluation of Reinforced Concrete Structures: Non-destructive Testing Methods*”. Woodhead Publishing Series in Civil and Structural Engineering, 2(35), Chapter 25, pp. 574–584.
11. Ranalli, D., Scozzafava, M., and Tallini, M. (2004). “*Ground Penetrating Radar Investigations for the Restoration of Historic Buildings: The Case Study of the Collemaggio Basilica (L’Aquila, Italy).*” Journal of Cultural Heritage, 5, pp. 91–99.
12. Solla, M., Lorenzo, H., Riveiro, B., and Rial, F.I. (2011). “*Non-destructive Methodologies in the Assessment of the Masonry Arch Bridge of Traba, Spain.*” Engineering Failure Analysis, 18, pp. 828–835.

13. Fenning, P.J. and McCannt, D.M. (1995). “*Sea Defences: Geophysical and NDT Investigation Techniques.*” NDT&E International, 28, pp. 359–366.
14. Minet, J., Wahyudi, A., Bogaert, P., Vanclooster, M., and Lambot, S. (2011). “*Mapping Shallow Soil Moisture Profiles at the Field Scale Using Full-waveform Inversion of Ground Penetrating Radar Data.*” Geoderma, 161, pp. 225–237.
15. Binda, L., Lenzi, G., and Saisi, A. (1998). “*NDE of Masonry Structures: Use of Radar Tests for the Characterisation of Stone Masonries.*” NDT&E International, 31, pp. 411–419.
16. Binda L., Zanzi, L., Lualdi, M., and Condoleo, P. (2005)., “*The use of georadar to assess damage to a masonry bell tower in Cremona, Italy.*” NDT E Int., 38(3), 171–179.
17. Diamanti, N. and Redman, D. (2012). “*Field Observations and Numerical Models of GPR Response from Vertical Pavement Cracks.*” Journal of Applied Geophysics, 81, pp. 106–116.
18. Helmerich, R., Niederleithinger, E., Trela, C., Bien, J., Kaminski, T., and Bernardini, G. (2012). “*Multi-tool Inspection and Numerical Analysis of an Old Masonry Arch Bridge.*” Structure and Infrastructure Engineering, 8, pp. 27–39.
19. Benedetto, A., Manacorda, G., Simi, A., and Tosti, F. (2012). “*Novel Perspectives in Bridges Inspection Using GPR.*” Non-destructive Testing and Evaluation, 27(3), pp. 239–251.
20. Hugenschmidt, J. and Mastrangelo, R. (2006). “*GPR Inspection of Concrete Bridges.*” Cement and Concrete Composites, 28, pp. 384–392.
21. Saarenketo, T. and Soderqvist, M.K. (1994). “Ground-penetrating Radar Applications for Bridge Deck Evaluations in Finland.” Insight, 36, pp. 496–501.
22. Diefenderfer, B., Galal, K., and Mokarem, D. (2005). “*Effect of Subsurface Drainage on the Structural Capacity of Flexible Pavement.*” Final Report No VTRC 05-R35, Virginia Transportation Research Council, Richmond, VA.
23. Benedetto, A. and Pensa, S. (2007). “*Indirect Diagnosis of Pavement Structural Damages Using Surface GPR Reflection Techniques.*” Journal of Applied Geophysics, 62, pp. 107–123.
24. Morey, R. (1998). “*Ground Penetrating Radar for Evaluating Subsurface Conditions for Transportation Facilities*”. Synthesis of Highway Practice 255, National Cooperative Highway Research Program, Transportation Research Board, National Academy Press.
25. Daniels, D.J. (2004). *Ground Penetrating Radar (2nd ed.)*. Knoval (Institution of Engineering and Technology), pp. 1–4. ISBN 978-0-86341-360-5.
26. Topp, G.C., Davis, J.L., and Annan, A.P. (1980). “*Electromagnetic Determination of Soil Water Content: Measurements in Coaxial Transmission Lines.*” Water Resources Research, 16(3), pp. 574–582.

27. Saarenketo, T. (1997). “*Using Ground-Penetrating Radar and Dielectric Probe Measurements in Pavement Density Quality Control.*” Transportation Research Record: Journal of the Transportation Research Board, 1575, Transportation Research Board of the National Academies, Washington, DC, pp. 34–41.
28. Al-Qadi, I.L., Leng, Z., Lahouar, S., and Baek, J. (2010). “*In-Place Hot-Mix Asphalt Density Estimation Using Ground-Penetrating Radar.*” Transportation Research Record: Journal of the Transportation Research Board, 2152(1), Transportation Research Board of the National Academies, Washington, DC, pp. 19–27.
29. Al-Qadi, I.L., Lahouar, S., and Loulizi, A. (2003). “*Successful Application of Ground-Penetrating Radar for Quality Assurance–Quality Control of New Pavements.*” Transportation Research Record: Journal of the Transportation Research Board, 1861, Paper No. 03-3512, Transportation Research Board of the National Academies, Washington, DC.
30. Al-Qadi, I.L. and Riad, S.M. (1996). “*Characterization of Portland Cement Concrete: Electromagnetic and Ultrasonic Measurement Techniques.*” Report Submitted to National Science Foundation, Washington, DC.
31. Sihvola, A. (1999), “*Electromagnetic Mixing Formulas and Applications*”. Institute of Electrical Engineers, IEEE Publishing, London.
32. American Association of State Highway and Transportation Officials (AASHTO). (1993). *Guide for Design of Pavement Structures*. Washington, DC.
33. Abdelmawla, A.M. and Kim, S. (2020). “*Application of Ground Penetrating Radar to Estimate Subgrade Soil Density.*” Infrastructures, 5(2), p. 12.
34. Ceylan, H., Gopalakrishnan, K., and Guclu, A. (2007). “*Advanced Approaches to Characterizing Nonlinear Pavement System Responses.*” Transportation Research Record: Journal of the Transportation Research Board, 2005, Transportation Research Board of the National Academies, Washington, DC, pp. 86–94.
35. Zaghloul, S. and White, T. (1993). “*Use of a Three-dimensional, Dynamic Finite Element Program for Analysis of Flexible Pavement.*” Transportation Research Record: Journal of the Transportation Research Board, 1388, Transportation Research Board of the National Academies, Washington, DC, pp. 60–69.
36. Saltan, M. and Karasahin, M. (2006). “*A Finite Element Based Back calculation Program for Flexible Pavements.*” Indian Journal of Engineering & Materials Sciences, 13, pp. 221–230.
37. Goktepe, A.B., Agar, E., and Lav, A.H. (2006). “*Advances in Back calculating the Mechanical Properties of Flexible Pavements.*” Advances in Engineering Software, 37, pp. 421–431.
38. Liang, R. and Zeng, S. (2002). “*Efficient Dynamic Analysis of Multilayered System During Falling Weight Deflectometer Experiments.*” Journal of Transportation Engineering, 128(4), pp. 366–374.

39. Gopalakrishnan, K., Kim, S., Ceylan, H., and Kaya, O. (2014). “*Development of Asphalt Dynamic Modulus Master Curve Using Falling Weight Deflectometer Measurements.*” TR-659, InTrans Project Reports, 69.
40. Meier, R.W. and Rix, G.J. (1995). “*Back calculation of Flexible Pavement Moduli from Falling Weight Deflectometer Data Using Artificial Neural Networks.*” Transportation Research Record: Journal of the Transportation Research Board, 1473, Transportation Research Board of the National Academies, Washington, DC, pp. 72–81.
41. Chatti, K., Ji, Y., and Harichandran, R. (2004) “*Dynamic Time Domain Back calculation of Layer Moduli, Damping, and Thicknesses in Flexible Pavements.*” Transportation Research Record: Journal of the Transportation Research Board, 1869, Transportation Research Board of the National Academies, Washington, DC, pp. 106–116.
42. Varma, S., Kutay, M.E., and Levenberg, E. (2013). “*Viscoelastic Genetic Algorithm for Inverse Analysis of Asphalt Layer Properties from Falling Weight Deflections.*” Transportation Research Record: Journal of the Transportation Research Board, 2369, Transportation Research Board of the National Academies, Washington, DC, pp. 38–46.
43. Lee, H.S., Ayyala, D., and Quintus, H.V. (2017). “*Dynamic Back calculation of Viscoelastic Asphalt Properties and Master Curve Construction.*” Transportation Research Record: Journal of the Transportation Research Board, 2641, Transportation Research Board of the National Academies, Washington, DC, pp. 29–38.
44. Madsen, S.S. and Levenberg, E. (2018). “*Dynamic Back calculation with Different Load-time Histories.*” Road Materials and Pavement Design, 19(6), pp. 1314–1333.
45. Li, M. and Wang, H. (2018). “*Prediction of Asphalt Pavement Responses from FWD Surface Deflections Using Soft Computing Methods.*” Journal of Transportation Engineering, 144(2).
46. Berenger, J. (1994). “*A Perfectly Matched Layer for the Absorption of Electromagnetic Waves.*” Journal of Computational Physics, 114(2), pp. 185–200.
47. Madsen, S.S., Krenk, S., and Hededal, O. (2013). “*Perfectly Matched Layer (PML) for Transient Wave Propagation in a Moving Frame of Reference.*” 4th ECCOMAS Thematic Conference on Computational Methods in Structural Dynamics and Earthquake Engineering, Kos Island, Greece, June 12–14.
48. Kohno, H., Bathe, K.J., and Wright, J.C. (2010). “*A Finite Element Procedure for Multiscale Wave Equations with Applications to Plasma Waves.*” Computers and Structures, 88, pp. 87–94.
49. Ham, S. and Bathe, K.J. (2012). “*A Finite Element Method Enriched for Wave Propagation Problems.*” Computers and Structures, 94–95, pp. 1–12.
50. Thomson, W.T. (1950). “*Transmission of Elastic Waves Through a Stratified Solid Medium.*” Journal of Applied Physics, 21, pp. 89–93.
51. Haskell, N.A. (1953). “*The Dispersion of Surface Waves on Multilayered Media.*” Bulletin of Seismological Society of America, 43, pp. 17–34.

52. Kausel, E. and Roesset, J.M. (1981). “*Stiffness Matrices for Layered Soils.*” Bulletin of the Seismological Society of America, 71, pp. 1743–1761.
53. Rizzi, S.A. and Doyle, J.F. (1992). “*A Spectral Element Approach to Wave Motion in Layered Solids.*” Journal of Vibration and Acoustics, 114, pp. 569–577.
54. Doyle, J.F. (1997). “*Wave Propagation in Structures: Spectral Analysis Using Fast Discrete Fourier Transforms.*” Springer-Verlag, New York.
55. Al-Khoury, R., Scarpas, A., Kasbergen, C., and Blaauwendraad, J. (2001a). “*Spectral Element Technique for Efficient Parameter Identification of Layered Media. Part I. Forward Calculation.*” International Journal of Solids and Structures, 38, pp. 1605–1623.
56. Al-Khoury, R., Scarpas, A., Kasbergen, C., and Blaauwendraad, J. (2001b). “*Spectral Element Technique for Efficient Parameter Identification of Layered Media. Part II: Inverse Calculation.*” International Journal of Solids and Structures, 38, pp. 8753–8772.
57. Al-Khoury, R., Scarpas, A., Kasbergen, C., and Blaauwendraad, J. (2002). “*Spectral Element Technique for Efficient Parameter Identification of Layered Media. Part III: Viscoelastic Aspects.*” International Journal of Solids and Structures, 39, pp. 2189–2201.
58. Chatti, K. and Yun, K.K. (1996). “*SAPSI-M: Computer Program for Analyzing Asphalt Concrete Pavements Under Moving Arbitrary Loads.*” Transportation Research Record: Journal of the Transportation Research Board, 1539, Transportation Research Board of the National Academies, Washington, DC, pp. 88–95.
59. Ji, Y. (2005). “Frequency and Time Domain Back calculation of Flexible Pavement Layer Parameters.” Ph.D. thesis, Michigan State University, East Lansing, MI.
60. Zhang, W., Drescher, A., and Newcomb, D.E. (1997). “*Viscoelastic Analysis of Diametral Compression of Asphalt Concrete.*” Journal of Engineering Mechanics, 123, pp. 596–603.
61. Lee, H.S. (2013a). “A New Solution for Viscoelastic Wave Propagation of Layered Structures Subjected to an Impact Load.” International Journal of Pavement Engineering, 15, pp. 542–557.
62. Lee, H.S. (2013b). “Development of a New Solution for Viscoelastic Wave Propagation of Pavement Structures and Its Use in Dynamic Back calculation.” Ph.D. thesis, Michigan State University, East Lansing, MI.
63. Kabanikhin, S.I. (2008). “*Definitions and Examples of Inverse and Ill-posed Problems.*” Journal of Inverse and Ill-Posed Problems, 17, pp. 317–357.
64. Hua, X.G., Ni, Y.Q., and Ko, J.M. (2009). “*Adaptive Regularization Parameter Optimization in Output-Error-Based Finite Element Model Updating.*” Mechanical Systems and Signal Processing, 23, pp. 563–579.

65. Sivanesar, N., Kramer, S.L., and Mahoney, J.P. (1991). “*Advanced Back calculation Using a Nonlinear Least Squares Optimization Technique.*” Transportation Research Record: Journal of the Transportation Research Board, 1293, Transportation Research Board of the National Academies, Washington, DC, pp. 93–102.
66. Gould, N.I.M. and Toint, P.L. (2007). “FILTRANE, a Fortran 95 Filter-Trust-Region Package for Solving Nonlinear Least-Squares and Nonlinear Feasibility Problems.” ACM Transactions on Mathematical Software, 33, pp. 3–25.
67. More, J.J. and Sorensen, D.C. (1983). “*Computing a Trust Region Step.*” SIAM Journal on Scientific and Statistical Computing, 4(3), pp. 553–572.
68. Byrd, R.H. and Schnabel, R.B. (1988). “Approximate Solution of the Trust Region Problem by Minimization over Two-dimensional Subspaces.” Mathematical Programming, 40, pp. 247–263.
69. Branch, M.A. (1995). “Inexact Reflective Newton Methods for Large-scale Optimization Subject to Bound Constraints.”, Ph.D. thesis, Cornell University, Ithaca, NY.
70. Macconi, M., Morini, B., and Porcelli, M. (2009). “*A Gauss–Newton Method for Solving Bound-constrained Underdetermined Nonlinear Systems.*” Optimization Methods and Software, 24(2), pp. 219–235.
71. Branch, M.A., Coleman, T.F., and Li, Y. (1999). “A Subspace, Interior, and Conjugate Gradient Method for Large-scale Bound-constrained Minimization Problems.” SIAM Journal on Scientific Computing, 21, pp. 1–23.
72. Bellavia, S., & Riccietti, E. (2018). “*On an Elliptical Trust-Region Procedure for Ill-Posed Nonlinear Least-Squares Problems.*”, Journal of Optimization Theory and Applications, 178, 824-859.
73. Kim, S., Etheridge, M.S., Chorzepa, M., Kim, Y. (2019). “*Development of MEPDG Input Database for Asphalt Mixtures.*” Final Report No GDOT RP 16-19, Georgia Department of Transportation, GA.
74. Yang, J. (2021). *Large-scale WebGL-powered Geospatial Data Visualization Tool*. Kepler.Gl. Available online: <https://kepler.gl/>.
75. Tighe, S., Li, N.Y., Falls, L.C., and Haas, R. (2000). “*Incorporating Road Safety into Pavement Management.*” 79th Annual Meeting of the Transportation Research Board, Transportation Research Board National Research Council, pp. 1–10.